PROTEUS: A Coupled Iterative Force-Correction Immersed-Boundary Multi-Domain Cascaded Lattice Boltzmann Solver

ARTICLE IN PRESS

Computers and Mathematics with Applications ▮ (▮▮▮▮) ▮▮▮–▮▮▮

Contents lists available at ScienceDirect

Computers and Mathematics with Applications

journal homepage: www.elsevier.com/locate/camwa

PROTEUS: A coupled iterative force-correction immersed-boundary multi-domain cascaded lattice Boltzmann solver

E.J. Falagkaris *, D.M. Ingram, I.M. Viola, K. Markakis

Institute of Energy Systems, School of Engineering, The University of Edinburgh, Colin Maclaurin Rd, EH9 3DW, Edinburgh, UK

ARTICLE INFO

Article history:
Received 22 February 2017
Received in revised form 14 June 2017
Accepted 7 July 2017
Available online xxxx

Keywords:
Cascaded lattice Boltzmann method
Central-moment
Immersed boundary method
Iterative force-correction
Multi-Domain
Unsteady flows

ABSTRACT

Most realistic fluid flow problems are characterized by high Reynolds numbers and complex boundaries. Over the last ten years, immersed boundary methods that are able to cope with realistic geometries have been applied to Lattice-Boltzmann (LB) methods. These methods, however, have normally been applied to low Reynolds number problems. Here we present a novel coupling between an iterative force-correction immersed boundary (Zhang et al., 2016) and a multi-domain cascaded LB method. The iterative force-correction immersed boundary method has been selected due to the improved accuracy of the computation, while the cascaded LB formulation is used due to its superior stability at high Reynolds numbers. The coupling is shown to improve both the stability and numerical accuracy of the solution. The resulting solver has been applied to viscous flow (up to a Reynolds number of 100000) passed a NACA-0012 airfoil at a 10 degree angle of attack. Good agreement with results obtained using a body-fitted Navier–Stokes solver has been obtained. The formulation provides a straight forward and efficient method for modeling realistic geometries and could easily be extended to problems with moving boundaries.

1. Introduction

In computational fluid dynamics (CFD), the accurate and efficient treatment of complex and/or moving boundaries is a primary issue in the development of an appropriate numerical scheme. Various numerical methods with different numerical accuracy and computational cost have been developed to address this issue. This study will focus on the coupling of the immersed boundary method (IBM) with the cascaded lattice Boltzmann method (CLBM).

There exist a few methods that establish the consistency of the lattice-Boltzmann method (LBM) with regard to the Navier–Stokes equations (NSE). The multiscale expansion of Chapman and Cowling [1] is widely used to validate the consistency of a LBM numerical scheme [2,3]. More recently, Sone [4] and Junk et al. [5] presented an asymptotic analysis based on the Hilbert expansion, whereas, Asinari [6] used a procedure based on the Grad moment expansion [7]. The asymptotic analysis [5] shows that the evolution of some observable quantities of the LBM do not affect the asymptotic behavior of the method [8]. Therefore, the scattering operator can be chosen somehow arbitrarily as long as the required constraints are obeyed. Chen et al. [9] and Qian et al. [10] proposed the most common, single-relaxation-time (SRT) collision operator, which is based on the Bhatnagar–Gross–Krook (BGK) approximation [11]. d'Humières [12] heuristically presented a multiple-relaxation-time (MRT) operator based on the raw moment formulation of the distribution functions in order to enhance collisions. The collisions are performed in moment space, where each moment is allowed to relax towards its

* Corresponding author.
E-mail address: E.falagkaris@ed.ac.uk (E.J. Falagkaris).

http://dx.doi.org/10.1016/j.camwa.2017.07.016
0898-1221/

equilibrium state at a different rate. Thus, by carefully treating each relaxation time separately, the numerical stability is significantly improved. In addition, Ginzburgh and d'Humières [13] showed that the physical representation of certain problems can be further improved by imposing specific relaxation rates at certain non-hydrodynamics moments. However, it should be noted that this MRT formulation [12] is not unique [14]. Another class of collision operators was developed [15,16] based on a minimization solution of Boltzmann's H-function.

Most recently, Geier et al., [17,18], by realizing the insufficient level of Galilean invariance of the previous MRT operators, introduced the cascaded LBM in which collisions are performed in a reference frame shifted by the macroscopic velocity, where central moments are allowed to relax at different rates in a cascaded manner. Thus, allowing the evolution of higher-order moments to depend on both lower-order moments and hydrodynamic variables, leads to using a discrete equilibrium distribution that contains higher order terms in velocity. In previous SRT and MRT models, the discrete equilibrium distribution was derived under the low Mach, i.e second-order, approximation of the continuous Maxwell–Boltzmann distribution. This approximation is equivalent to a large-wavelength assumption which is incorrect since most instabilities arise from small-wavelength patterns [17,18]. Furthermore, in order to uniquely determine the equilibrium distribution and achieve Galilean invariance, a given velocity set must be sufficient to adjust different moments independently. Therefore, the common 13, 15 and 19 velocity sets used in three-dimensional LBMs are not applicable in the CLBM formulation. As a further improvement to the 3D CLBM, Geier et al. [19] proposed a novel scheme, where collisions are carried out in the space of cumulants. The use of cumulants is shown to eliminate errors in Galilean invariance and hyper-viscosity while maintaining, or even improve, the stability of the central moment method.

Most practical problems involving complex geometries often require unstructured body-conformal grids in order to accurately enforce the boundary conditions. Such approaches involve complicated meshing techniques and increase both the CPU time and the amount of memory used. The solution process can be simplified by developing a non-body-conformal approach where the solution of the governing fluid equations is decoupled from the implementation of the boundary conditions. The immersed boundary method is such an approach and it was initially introduced by Peskin [20] in the 1970s to simulate blood flows in the human heart. In recent years, the IBM has received a great attention in simulating flows with complex geometries [21–24]. IBM uses a fixed Eulerian grid, usually a Cartesian grid, for the fluid and a Lagrangian set of points, independent of the first, to represent the immersed physical boundary. The boundary is treated as a deformable body with high stiffness, thus a small distortion on the boundary will yield a force that tends to restore the boundary to its original position. The total balanced force is then distributed into the Eulerian grid and the NSE with a body force term are solved for the entire computational domain. Conceptually, the boundary force density in the IBM can be evaluated by either feedback forcing methods or by direct forcing methods.

In recent years, many efforts have been made in order to improve the coupling between the IBM and the LBM. For rigid boundaries, Feng and Michaelides [25] proposed a penalty method, allowing a small deformation of the boundary's position which is restored using a linear spring approximation. Dupuis et al. [26] presented a direct-forcing IBM. The force is computed using the interpolated IB and a reference velocity. The momentum exchange method of the particle distributions was used by Niu et al. [27] to calculate the force acting on the immersed boundary. For deformable boundary configurations, Zhang et al. [28] proposed an IB-LBM scheme to investigate the aggregation of red blood cells, whereas Cheng and Zhang [29] improved the forcing introducing method. However, none of the above methods can satisfy the non-slip boundary condition exactly, since the velocity correction is pre-calculated and cannot be further manipulated. Wu and Shu [30] developed an implicit velocity correction-based IB-LBM based on Guo's external forcing term [31]. In the present study, the iterative force correction IB scheme proposed by Zhang et al. [32] is used.

This paper focuses on the coupling between the IBM and the central moment formulation of the LBM. We investigate how the iterative force correction IB scheme affects the overall accuracy compared to the established multi-direct-forcing (MDF-IB) formulation. For the implementation of the MDF-CLBM scheme, the developments made by Premnath et al. [33] on the collision operator are used. The paper is organized as follows. In Section 2, the numerical method is presented. That includes, the central-moment formulation of the LBM and the selection of the discrete forcing term, the iterative force-correction algorithm and the coupling with the CLBM, as well as the multi-domain algorithm and the domain boundary conditions used in the present study. Numerical results and the accuracy and robustness of the proposed scheme are reported in Section 3. Finally, the conclusions are summarized in Section 4.

2. Numerical method

2.1. The cascaded lattice-Boltzmann method

2.1.1. Basic formulation of the LBM with the central-moment collision operator

Consider a two-dimensional athermal fluid and let only the density $\rho(x, y)$, the velocity $\mathbf{u} = (u_x, u_y)$, and the external forces $\mathbf{F}(x, y)$, to characterize its local hydrodynamic behavior at a Cartesian coordinate system (x, y). For two-dimensional flows, the nine-velocity square lattice model, denoted as D2Q9 [10], has been successfully used in the literature [34]. The discrete evolution equation for the CLBM with external forcing may be written as

$$f_\alpha(\mathbf{x} + \mathbf{e}_\alpha \delta t, t + \delta t) = f_\alpha(\mathbf{x}, t) + \Omega_a(\mathbf{x}, t) + \delta t S_a, \tag{1}$$

Please cite this article in press as: E.J. Falagkaris, et al., PROTEUS: A coupled iterative force-correction immersed-boundary multi-domain cascaded lattice Boltzmann solver, Computers and Mathematics with Applications (2017), http://dx.doi.org/10.1016/j.camwa.2017.07.016.

where $\mathbf{e}_\alpha : \alpha = 0, 1, \ldots, 8$ is the discrete velocity set; $f_\alpha(\mathbf{x}, t) : \alpha = 0, 1, \ldots, 8$ are the discrete particle distribution functions (PDF) at time t and position $\mathbf{x}$; $\Omega_\alpha(\mathbf{x}, t) : \alpha = 0, 1, \ldots, 8$ is the discrete collision operator, and $S_\alpha(\mathbf{x}, t) : \alpha = 0, 1, \ldots, 8$ are the discrete forcing terms. Collision is described as a cascaded process in which the higher order moments are influenced by the collision effects on the lower order moments. Using Geier's [17] notation, the collision operator takes the form $\Omega_a = (\mathbf{K} \cdot \hat{\mathbf{k}})_a$, where $\mathbf{K}$ is the transformation matrix [18,33], and $\hat{\mathbf{k}} = \hat{k}_a(\mathbf{x}, t) : \alpha = 0, 1, \ldots, 8$ are the moments of the distribution functions. Premnath et al. [33] incorporated the forcing terms in the central-moment collision operator and derived analytical expressions for the discrete forces and their moments. The general expression of the collision kernel without the integrated force terms is of the form

$$\hat{k}_0 = \hat{k}_1 = \hat{k}_2 = 0, \tag{2}$$

$$\hat{k}_3 = \omega_3 \frac{1}{12}\Big\{-(f_1 + f_2 + f_3 + f_4 + 2(f_5 + f_6 + f_7 + f_8)) + \frac{2}{3}\rho + \rho(u_x^2 + u_y^2)\Big\}, \tag{3}$$

$$\hat{k}_4 = \omega_4 \frac{1}{4}\Big\{(f_2 + f_4 - f_1 - f_3) + \rho(u_x^2 - u_y^2)\Big\}, \tag{4}$$

$$\hat{k}_5 = \omega_5 \frac{1}{4}\Big\{(f_5 + f_7 - f_6 - f_8) - \rho u_x u_y\Big\}, \tag{5}$$

$$\begin{aligned}\hat{k}_6 = \omega_6 \frac{1}{4}\Big\{&(f_5 + f_6 - f_7 - f_8 - 2u_x(f_5 + f_7 - f_6 - f_8) - u_y(f_1 + f_3 + f_5 + f_6 + f_7 + f_8)) \\ &+ 2\rho u_x^2 u_y\Big\} - 2u_x\hat{k}_5 - \frac{1}{2}u_y(3\hat{k}_3 + \hat{k}_4),\end{aligned} \tag{6}$$

$$\begin{aligned}\hat{k}_7 = \omega_7 \frac{1}{4}\Big\{&(f_5 + f_8 - f_6 - f_7 - 2u_y(f_5 + f_7 - f_6 - f_8) - u_x(f_2 + f_4 + f_5 + f_6 + f_7 + f_8)) \\ &+ 2\rho u_x u_y^2\Big\} - 2u_y\hat{k}_5 - \frac{1}{2}u_y(3\hat{k}_3 + \hat{k}_4),\end{aligned} \tag{7}$$

$$\begin{aligned}\hat{k}_8 = \omega_8 \frac{1}{4}\Big\{&-(f_5 + f_6 + f_7 + f_8 - 2u_x(f_5 + f_8 - f_6 - f_7) - 2u_y(f_5 + f_6 - f_7 - f_8) \\ &+ u_x^2(f_2 + f_4 + f_5 + f_6 + f_7 + f_8) + u_y^2(f_1 + f_3 + f_5 + f_6 + f_7 + f_8) + 4u_x u_y(f_5 + f_7 - f_6 - f_8)) \\ &+ \frac{1}{9}\rho + 3\rho u_x^2 u_y^2\Big\} - 2\hat{k}_3 - \frac{1}{2}u_x^2(3\hat{k}_3 - \hat{k}_4) - \frac{1}{2}u_y^2(3\hat{k}_3 + \hat{k}_4) - 4u_x u_y\hat{k}_5 - 2u_y\hat{k}_6 - 2u_x\hat{k}_7,\end{aligned} \tag{8}$$

where $\omega_\alpha : \alpha = 3, 4, \ldots, 8$ are the relaxation parameters for the different moments. A Chapman–Enskog multiscale analysis shows that the kinematic shear viscosity is determined by the relaxation parameters ω_4 and ω_5. The constraint $\omega_4 = \omega_5$ occurs from the requirement of maintaining an isotropic stress tensor. Since the kinematic shear viscosity is a function of the speed of sound and the mean free flight time between two binary collisions, it is given by

$$\nu = c_s^2\left(\omega_{(4,5)}{}^{-1} - 0.5\right), \tag{9}$$

where $c_s = 1/\sqrt{3}$ is the speed of sound for the D2Q9 model. The bulk viscosity is determined by the relaxation parameter ω_3. Geier [17], performed various numerical simulations in order to find consistent relaxation rates to match higher order moments to physical quantities. A stable numerical approach is to equilibrate higher-order moments, i.e. taking $\omega_6 = \omega_7 = \omega_8 = 1$.

Finally, the hydrodynamic variables, fluid density and velocity, are obtained by taking the zeroth and first moments of the distributions as

$$\rho = \sum_\alpha^q f_\alpha = \langle f_\alpha | \rho \rangle, \qquad \rho u_i = \sum_\alpha^q f_\alpha e_{\alpha i} = \langle f_\alpha | e_{\alpha i} \rangle, \quad i \in x, y. \tag{10}$$

2.1.2. Cheng's formulation of the discrete external force term

The discrete forcing term S_α in Eq. (1) can have various expressions. Both the stability and the accuracy of a simulation rely upon the form of the external forcing term. Cheng and Li [35] proposed a term that does not modify the macroscopic velocity in Eq. (10) and can handle both space and time dependent forces:

$$S_\alpha = 0.5[s_\alpha(\mathbf{x} + \mathbf{e}_\alpha \delta t, t + \delta t) + s_\alpha(\mathbf{x}, t)], \tag{11}$$

$$s_\alpha = w_\alpha\left\{A + 3\mathbf{B} \cdot [(\mathbf{e}_\alpha - \mathbf{u}) + 3(\mathbf{e}_\alpha \cdot \mathbf{u})\mathbf{e}_\alpha]\right\}. \tag{12}$$

We take $A = 0$ and $\mathbf{B} = \mathbf{F} = (F_x, F_y)$. Eqs. (11)–(12) are used in the iterative immersed boundary treatment as described in 2.3.

Please cite this article in press as: E.J. Falagkaris, et al., PROTEUS: A coupled iterative force-correction immersed-boundary multi-domain cascaded lattice Boltzmann solver, Computers and Mathematics with Applications (2017), http://dx.doi.org/10.1016/j.camwa.2017.07.016.

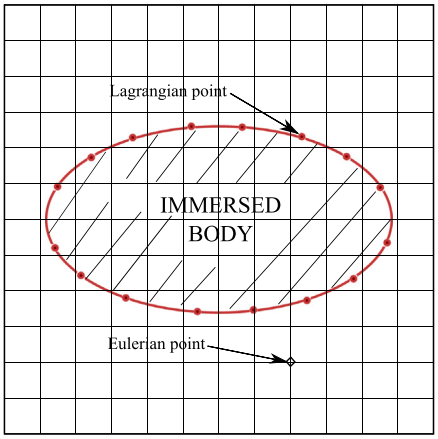

Fig. 1. Immersed boundary illustration using a set of Lagrangian points to represent the boundary and a set of Eulerian points defined by the intersection points of the mesh lines to represent the fluid domain.

2.2. The immersed boundary method—basic formulation

Consider a closed curve $\mathscr{E}(t)$ immersed in a two-dimensional fluid domain $\Omega(t)$ as shown in Fig. 1. For viscous incompressible flows, the governing equations of the immersed boundary formulation are formulated as

$$\nabla \cdot \mathbf{u} = 0, \tag{13}$$

$$\rho\left(\frac{\partial \mathbf{u}}{\partial t} + \mathbf{u}\cdot\nabla\mathbf{u}\right) + \nabla p = \mu\triangle\mathbf{u} + \mathbf{g}, \tag{14}$$

$$\mathbf{g}(\mathbf{x}, t) = \int_{\mathscr{E}} \mathbf{G}(s, t)\delta(\mathbf{x} - \mathbf{X}_{\mathscr{L}}(s, t))ds, \tag{15}$$

$$\frac{\partial \mathbf{X}_{\mathscr{L}}(s, t)}{\partial t} = \mathbf{U}(\mathbf{X}_{\mathscr{L}}(s, t), t) = \int_{\mathscr{E}} \mathbf{u}(\mathbf{x}, t)\delta(\mathbf{x} - \mathbf{X}_{\mathscr{L}}(s, t))d\mathbf{x}, \tag{16}$$

$$\mathbf{G}(s, t) = \mathbf{S}(\mathbf{X}_{\mathscr{L}}(s, t), t). \tag{17}$$

Eqs. (13)–(14) are the Eulerian Navier–Stokes equations with external forces $\mathbf{g}$ for the fluid domain $\Omega(t)$, whereas Eqs. (15)–(17) are the equations in Lagrangian formalism for the immersed boundary $\mathscr{E}(t)$. $\mathbf{X}_{\mathscr{L}}$, $\mathbf{U}$, $\mathbf{G}$ are the position of the IB in Lagrangian coordinates, the IB velocity and force density, respectively. $\mathbf{x}$, $\mathbf{u}$, $\mathbf{g}$, ρ and p are the Cartesian coordinates, fluid velocity, external force density, density and pressure, respectively. δ is the delta function which can be expressed as a product of 1-Dimensional functions $\delta_h(\mathbf{x}-\mathbf{X}_{\mathscr{L}}) = h^{-d}\prod_{i=1}^{d}\phi\left(\frac{x^i - X_{\mathscr{L}}{}^i}{h}\right)$, where d is the dimensionality of the problem and h is the grid spacing. In this study, the smoothed 4-point delta function [36], $\phi_4^*(r)$, will be used for the force spreading in Eq. (15) and the Lagrange polynomials for the velocity interpolation, $U_{l(\mathbf{x}_l,t)}$, in Eq. (16). This selection is based upon the observations of Zhang et al. [32] and Cheng et al. [37].

$$\phi_4^*(r) = \begin{cases} \dfrac{3}{8} + \dfrac{\pi}{32} - \dfrac{r^2}{4} & \text{if } |r| \le 0.5 \\ \dfrac{1}{4} + \dfrac{1-|r|}{8}\sqrt{-2+8|r|-4r^2} - \dfrac{1}{8}\arcsin(\sqrt{2}(|r|-1)) & \text{if } 0.5 \le |r| \le 1.5 \\ \dfrac{17}{16} - \dfrac{\pi}{64} - \dfrac{3|r|}{4} + \dfrac{r^2}{8} + \dfrac{|r|-2}{16}\sqrt{-14+16|r|-4r^2} & \text{if } 1.5 \le |r| \le 2.5 \\ 0 & \text{if } 2.5 \le |r|, \end{cases} \tag{18}$$

$$U_{l(\mathbf{x}_l,t)} = \sum_{ij}\left(\prod_{m=1,m\neq i}^{i_{\max}} \frac{X_l - x_{mj}}{x_{ij} - x_{mj}}\right)\left(\prod_{n=1,n\neq j}^{j_{\max}} \frac{Y_l - y_{in}}{y_{ij} - y_{in}}\right)u_{ij}(\mathbf{x} + \mathbf{e}_a\delta t, t + \delta t), \quad l = \mathscr{L}. \tag{19}$$

2.3. Coupling schemes

In this study, the iterative force correction IB scheme proposed by Zhang et al. [32] is coupled with the CLBM. A few iterative IB schemes exist in the literature [38,39]. Most recently, De Rosis and Leveque [40] combined the CLBM with the

Please cite this article in press as: E.J. Falagkaris, et al., PROTEUS: A coupled iterative force-correction immersed-boundary multi-domain cascaded lattice Boltzmann solver, Computers and Mathematics with Applications (2017), http://dx.doi.org/10.1016/j.camwa.2017.07.016.

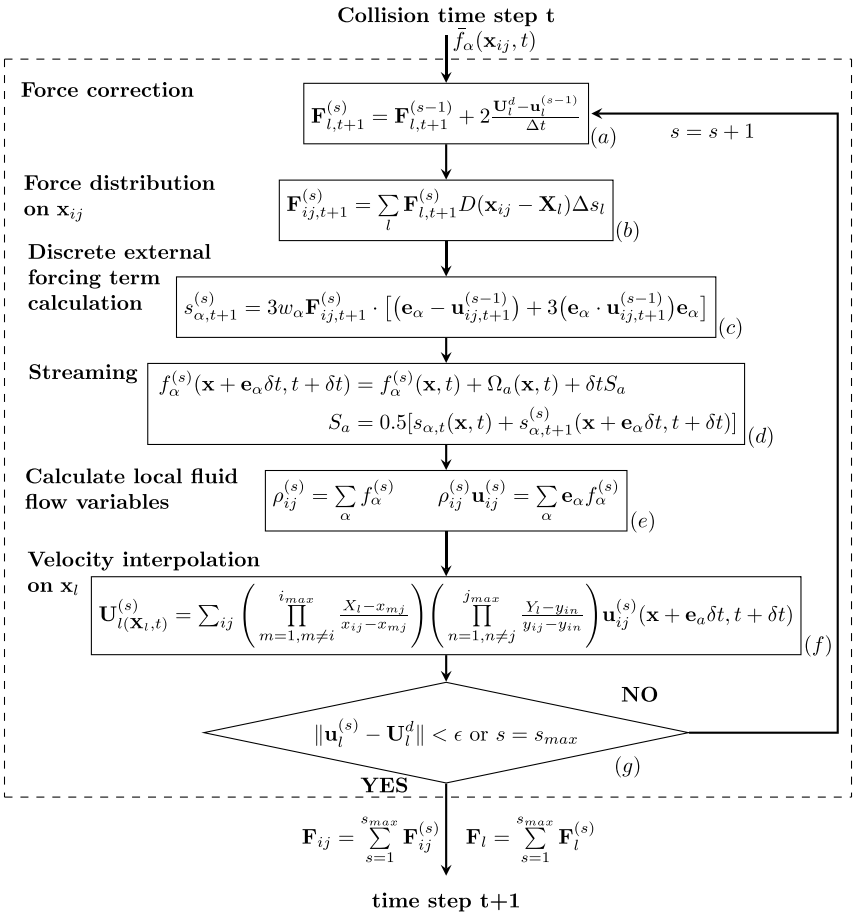

Fig. 2. Computational algorithm of the iterative force correction IBM.

scheme proposed by Inamuro [39]. However, these methods explicitly modify the velocity term in Eq. (10). Therefore, the overall accuracy of the surrounding flow field rather deteriorates as the number of iterations in the IBM increases.

Kang [38] reported a similar result. A different approach is used in the present work. Following Cheng and Li's approach [35], the external forcing term in Eq. (1) is split into two parts: the effects on the current and the next time step, Eq. (11). Instead of using an implicit method, an iterative scheme is proposed to predict the forcing term at the next time step and no modification of the velocity term in Eq. (10) is necessary. Both the velocity and the density are corrected iteratively by directly incorporating the forcing term at the next time step in the PDFs. For the analytical derivation of this scheme the reader should refer to [32,35]. The proposed scheme is compared with the MDF-CLBM scheme. The developments made by Premnath et al. [33] on the collision operator along with the multi-direct-forcing IBM [38] are used for the latter. Fig. 2 shows the computational algorithm for the iterative force correction IB algorithm of Zhang et al. [32] used in this work.

2.4. Multi-domain algorithm

In order to increase the solution accuracy around the area of interest, whilst maintaining a non-prohibitive computational cost, a grid refinement technique is employed in this study. There exist two major grid refinement approaches in the LBM. In the first one, the flow variables are represented using a volumetric cell-centered method [41–43], while in the second, a point-wise, cell-vertex approach is used [44,45]. Filippova and Hanel [44] used an adjustment of the non-equilibrium distributions based on the different relaxation times of each grid level in order to transfer information between grids with different resolution, whilst keeping an equal Reynolds number in all grids. Lagrava et al. [46] proposed a method of the same principle, where a filtering operation was employed when transferring information from fine to coarse grids, where the fine grid scales that cannot be resolved by the coarse grid are removed. In this work, the latter approach is considered. We only present the computational procedure and some differences with respect to the original implementation. For more details, the reader should refer to [46].

Please cite this article in press as: E.J. Falagkaris, et al., PROTEUS: A coupled iterative force-correction immersed-boundary multi-domain cascaded lattice Boltzmann solver, Computers and Mathematics with Applications (2017), http://dx.doi.org/10.1016/j.camwa.2017.07.016.

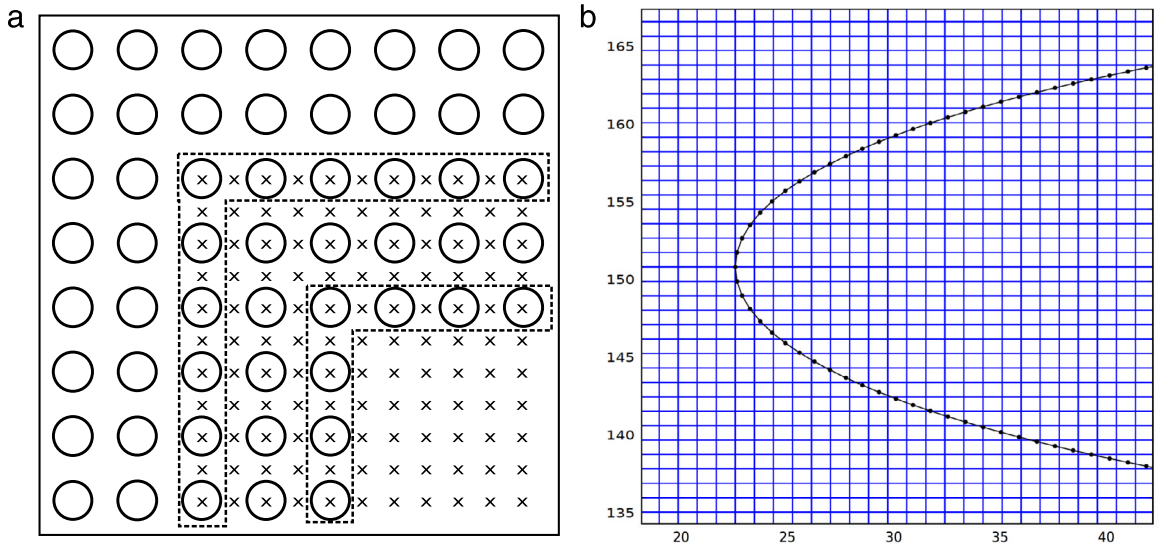

Fig. 3. (a) Overlapping region between fine and coarse grids. The dot enclosed areas indicate the exchange of information interfaces between two consecutive grid levels. The overlapping interface is five fine grid spacings wide to allow for a smoother transition of the information exchange. (b) A typical fine grid around the leading edge of a NACA-0012 airfoil.

The overlapping between a fine and a coarse grid is illustrated in Fig. 3a. The interface between two grids is two coarse grid spacings in order to allow for a smoother information exchange at unsteady flows. Fig. 3b shows a typical grid around the leading edge of a NACA 0012 airfoil with $\delta x = 1/c$ and $c = 400\ lu$ (lattice units) where c is the chord of the foil. The computational multi-domain algorithm is described below.

1. Initialize ρ and $\mathbf{u}$ on every domain and compute the equilibrium distributions f_i^{eq}.
2. Collide and Stream all distributions on the coarse grid. The coarse grid is now at time $t + \delta t_c$.
3. Collide and Stream once on the fine grid bringing it to time $t + \delta t_c/2$.
4. Perform a linear temporal interpolation of ρ_c, $\mathbf{u}_c$ and $f_{i,c}^{neq}$ at time $t + \delta t_c/2$ at the fine-coarse interface.
5. Spatially interpolate the values $\rho_c(t + \delta t_c/2)$, $\mathbf{u}_c(t + \delta t_c/2)$ and $f_{i,c}^{neq}(t + \delta t_c/2)$ at the fine nodes with no overlapping coarse nodes.
6. All populations at the fine grid boundaries are reconstructed following a convective scaling.
7. Collide and Stream once on the fine grid bringing it to time $t + \delta t_c$.
8. Spatially interpolate the values $\rho_c(t + \delta t_c)$, $\mathbf{u}_c(t + \delta t_c)$ and $f_{i,c}^{neq}(t + \delta t_c)$ as in step 5.
9. All populations at the fine grid boundaries are reconstructed following a convective scaling.
10. Save the equilibrium and non-equilibrium distributions $f_{i,f}^{eq}, f_{i,f}^{neq}$ at the coarse-fine interface.
11. Replace all the populations at the coarse-fine interface using filtering and scaling.
12. Proceed to the next time-step. Go to step 2.

This algorithm describes the coupling between two grid resolution levels. If more resolution levels exist, a recursive algorithm based on the same principle of information exchange should be used. In this study, the computational domain is described with nine levels of refinement. A symmetric, cubic spline fitting is used for the spatial interpolation in steps 5 and 8 in order to eliminate any spatial asymmetries.

$$f(x) = \alpha_i + \beta_i x + \gamma_i x^2 + \delta_i x^3, \quad x_{i-1} \le x_i \le x_{i+1}. \tag{20}$$

The tridiagonal systems of equations are solved using the Thomas algorithm under the restrictions of nodal continuity of the function $f(x)$ and its first and second derivatives, as well as zero second derivative $f''(x)$ at the end nodes. The reader should refer to Tölke and Krafczyk [47] for a different approach. In step 11, we follow the filtering process proposed by Pellerin et al. [48], where both the equilibrium and nominal distributions are filtered using the values at the nine neighboring grid points.

$$\begin{aligned}\bar{f}_i(\mathbf{x}, t) = {} & 0.25 f_i(\mathbf{x}, t) + 0.125(f_i(\mathbf{x} + \mathbf{e}_1, t) + f_i(\mathbf{x} + \mathbf{e}_2, t) + f_i(\mathbf{x} + \mathbf{e}_3, t) + f_i(\mathbf{x} + \mathbf{e}_4, t)) \\ & + 0.0625(f_i(\mathbf{x} + \mathbf{e}_5, t) + f_i(\mathbf{x} + \mathbf{e}_6, t) + f_i(\mathbf{x} + \mathbf{e}_7, t) + f_i(\mathbf{x} + \mathbf{e}_8, t)),\end{aligned} \tag{21}$$

where the overbar denotes the filtered quantity. In this implementation, only the non-equilibrium part of the distributions that is proportional to the gradient of the velocity needs to be rescaled. Therefore, the scaling of the distributions in steps 6,

Please cite this article in press as: E.J. Falagkaris, et al., PROTEUS: A coupled iterative force-correction immersed-boundary multi-domain cascaded lattice Boltzmann solver, Computers and Mathematics with Applications (2017), http://dx.doi.org/10.1016/j.camwa.2017.07.016.

9 and 11 is described as

$$f_{i,c} = f_i^{eq}(\rho_f, \mathbf{u}_f) + \frac{2\omega_f}{\omega_c}\bar{f}_{i,f}^{neq}, \tag{22}$$

$$f_{i,f} = f_i^{eq,interpolated}(\rho_c, \mathbf{u}_c) + \frac{\omega_c}{2\omega_f}f_{i,c}^{neq,interpolated}. \tag{23}$$

What also differs from the work of Lagrava [46] is the equilibrium distribution function f^{eq}. Choosing the nominal moment basis and the orthogonalized matrix $\mathbf{K}$ [33], the equilibrium distribution contains higher order velocity terms as compared to the standard LBM [6].

$$f_0^{eq} = 4/9\rho - 2/3\rho(u_x^2 + u_y^2) + \rho u_x^2 u_y^2, \tag{24a}$$

$$f_1^{eq} = 1/9\rho + 1/3\rho u_x + 1/2\rho u_x^2 - 1/6\rho(u_x^2 + u_y^2) - 1/2\rho(u_x u_y^2 + u_x^2 u_y^2), \tag{24b}$$

$$f_2^{eq} = 1/9\rho + 1/3\rho u_y + 1/2\rho u_y^2 - 1/6\rho(u_x^2 + u_y^2) - 1/2\rho(u_y u_x^2 + u_x^2 u_y^2), \tag{24c}$$

$$f_3^{eq} = 1/9\rho - 1/3\rho u_x + 1/2\rho u_x^2 - 1/6\rho(u_x^2 + u_y^2) + 1/2\rho(u_x u_y^2 - u_x^2 u_y^2), \tag{24d}$$

$$f_4^{eq} = 1/9\rho - 1/3\rho u_y + 1/2\rho u_y^2 - 1/6\rho(u_x^2 + u_y^2) + 1/2\rho(u_y u_x^2 - u_x^2 u_y^2), \tag{24e}$$

$$f_5^{eq} = 1/36\rho + 1/12\rho(u_x + u_y + u_x^2 + u_y^2) + 1/4\rho(u_x u_y + u_x^2 u_y + u_x u_y^2 + u_x^2 u_y^2), \tag{24f}$$

$$f_6^{eq} = 1/36\rho + 1/12\rho(-u_x + u_y + u_x^2 + u_y^2) + 1/4\rho(-u_x u_y + u_x^2 u_y - u_x u_y^2 + u_x^2 u_y^2), \tag{24g}$$

$$f_7^{eq} = 1/36\rho + 1/12\rho(-u_x - u_y + u_x^2 + u_y^2) + 1/4\rho(u_x u_y - u_x^2 u_y - u_x u_y^2 + u_x^2 u_y^2), \tag{24h}$$

$$f_8^{eq} = 1/36\rho + 1/12\rho(u_x - u_y + u_x^2 + u_y^2) + 1/4\rho(-u_x u_y - u_x^2 u_y + u_x u_y^2 + u_x^2 u_y^2). \tag{24i}$$

2.5. Domain boundary conditions

A square computational domain $100c \times 100c$, where c is the characteristic length of the immersed body, is used in this study. The immersed body is located at the center of the domain. At the inlet, all particle distributions are reconstructed, following the regularization procedure of Latt and Chopard [49].

$$\hat{f}_\alpha = f_\alpha^{eq}(\rho, \mathbf{u}) + \frac{t_\alpha}{2c_s^4}\mathbf{Q}_\alpha : \mathbf{\Pi}^{(neq)}, \tag{25}$$

where the tensors $\mathbf{Q}_\alpha$ and $\mathbf{\Pi}^{(neq)}$ are defined as $\mathbf{Q}_\alpha = \mathbf{e}_\alpha\mathbf{e}_\alpha - c_s^2\mathbf{I}$ and $\mathbf{\Pi}^{(neq)} = \sum_{\alpha=0}^{q-1}\mathbf{e}_\alpha\mathbf{e}_\alpha(f_\alpha - f_\alpha^{eq})$. $\mathbf{I}$ is the identity matrix. The unknown populations in the tensor $\mathbf{\Pi}^{(neq)}$ are computed by using the bounce back of off-equilibrium parts rule $f_\alpha^{(neq)} = f_{opp(\alpha)}^{(neq)}$ [50]. At the outlet, an extrapolation in space and time is applied for the missing distributions. Assuming only waves normal to the boundary [19], the missing distributions are computed as

$$f_\alpha(\mathbf{x}, t) = f_\alpha(\mathbf{x} - \delta x, t - \delta t)\big(c_s - \mathbf{u}(\mathbf{x}, t - \delta t)\big)\delta t/\delta x + \big(1 - \big(c_s - \mathbf{u}(\mathbf{x}, t - \delta t)\big)\delta t/\delta x\big)f_\alpha(\mathbf{x}, t - \delta t). \tag{26}$$

Slip boundary conditions are used for the top and bottom sides of the domain. Following the work of Xu and Sagaut [51], absorbing layers are used in all domain boundaries, in order to damp and minimize the reflection of the acoustic waves. The right hand side of Eq. (1) needs to be modified according to

$$f_\alpha(\mathbf{x} + \mathbf{e}_\alpha\delta t, t + \delta t) = f_\alpha(\mathbf{x}, t) + \Omega_a^*(\mathbf{x}, t) + \delta t S_a + \delta t H_\alpha^{eq}(\rho^f, \mathbf{u}^f, \rho^*, \mathbf{u}^*, t), \tag{27}$$

where $H_\alpha^{eq}(\rho^f, \mathbf{u}^f, \rho^*, \mathbf{u}^*, t) = \chi\left(f_\alpha^{eq}(\rho^f, \mathbf{u}^f, t) - f_\alpha^{eq}(\rho^*, \mathbf{u}^*, t)\right)$ with $\chi = \sigma(x)$ being the strength of the absorbing layer, Fig. 4b. The superscript f denotes the farfield values of the velocity and density, whereas the superscript $*$ denotes the parametrized density $\rho^* = \sum_\alpha f_\alpha + n\delta t\sum_\alpha H_\alpha^{eq}(\rho^f, \mathbf{u}^f, \rho, \mathbf{u}, t)$ and velocity $\rho^* u_j^* = \sum_\alpha e_{\alpha j} f_\alpha + m\delta t\sum_\alpha e_{\alpha j} H_\alpha^{eq}(\rho^f, \mathbf{u}^f, \rho, \mathbf{u}, t)$ [31]. $m = n = 1/2$ as in [51].

3. Computational results

3.1. Numerical test of overall accuracy

Lattice Boltzmann methods are second-order accurate in time and space. However, since the interpolation steps in the immersed boundary method are only first order accurate in space, the effect on the global accuracy of the solution must be investigated. To evaluate the accuracy of the proposed IDF-CLBM coupling scheme, the two-dimensional unsteady and fully periodic Taylor–Green vortex flow in a square box is investigated. The analytical solutions for the velocity and pressure are of the form:

$$\mathbf{u}(\mathbf{x}, t) = U_0 \begin{Bmatrix} -\sqrt{k_y/k_x}\cos(k_x x)\sin(k_y y) \\ \sqrt{k_y/k_x}\sin(k_x x)\cos(k_y y) \end{Bmatrix} e^{-t/t_d}, \tag{28}$$

Please cite this article in press as: E.J. Falagkaris, et al., PROTEUS: A coupled iterative force-correction immersed-boundary multi-domain cascaded lattice Boltzmann solver, Computers and Mathematics with Applications (2017), http://dx.doi.org/10.1016/j.camwa.2017.07.016.

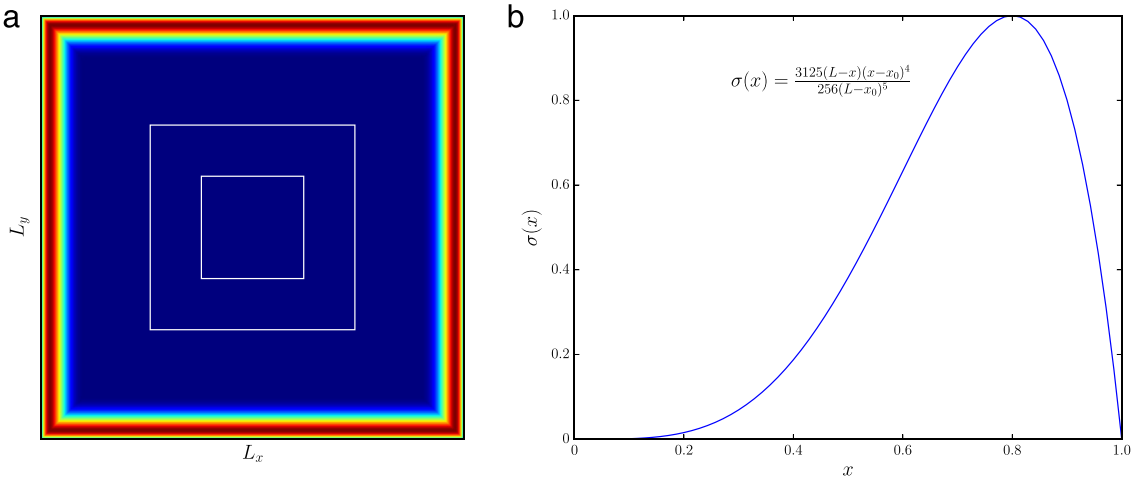

Fig. 4. (a) 2D computational domain with absorbing layer. (b) Normalized absorbing strength profile $\sigma(x)$ with $x_0 = 0$ and $L = 1$.

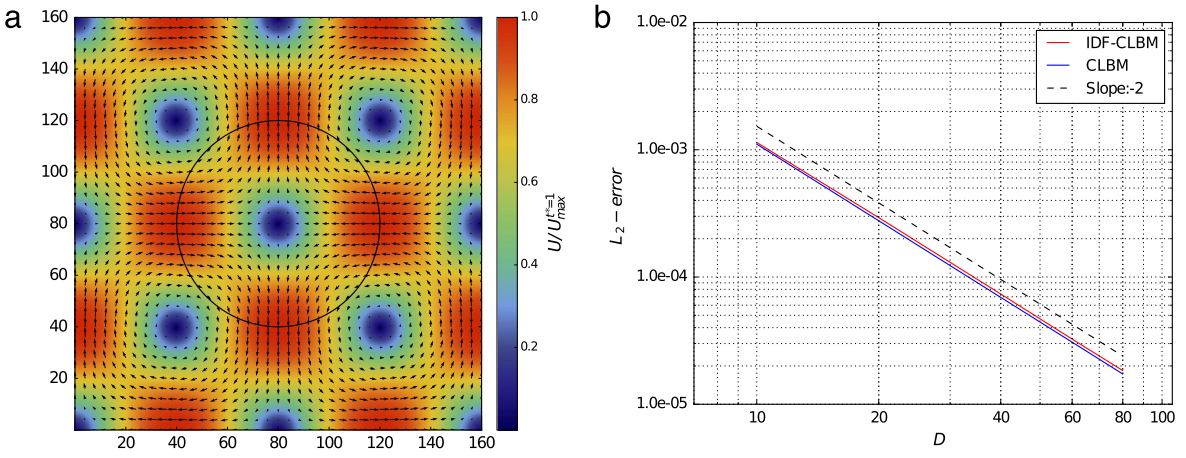

Fig. 5. (a) Velocity magnitude and vector plots at $t^* = 1$ resulting from the IDF-CLBM scheme. (b) Overall accuracy of the IDF-CLBM scheme.

$$p(\mathbf{x}, t) = p_0 - \rho U_0^2/4\left[k_y/k_x \cos(2k_x x) + k_x/k_y \cos(2k_y y)\right]e^{-2t/t_d}, \tag{29}$$

where U_0 is the initial velocity, $k_x = k_y = 2\pi/L$ are the wave vector $\mathbf{k}$ components and $t_d = [\nu(k_x^2 + k_y^2)]^{-1}$ is the decay time of the vortex. A circle with diameter $D = 0.5L$ is immersed at the center of square domain $L \times L$. Eqs. (28)–(29) are used for the initialization of the flow field. The prescribed velocity on the immersed circle is given by Eq. (28). Similar to the work of Wu and Shu [30], the Reynolds number is taken as $Re = U_0 D/\nu = 10$ and the single relaxation time is set to be $\tau = 0.65$. Four sets of grids are used, $L = 20, 40, 80, 160$. The global error of the velocities is evaluated at time $t^* = tD/U_\infty$ using the following L_2 norm error:

$$L_2^{error} \equiv \sqrt{\left(\sum (u_x^c - u_x^a)^2 + (u_y^c - u_y^a)^2\right)/N}, \tag{30}$$

where the summation is over the total number of grid nodes N and the superscripts, a and c, refer to the analytical and computational values respectively. The velocity magnitude and vector plots at $t^* = 1$ are shown in Fig. 5a. The global L_2-error versus the number of grid points along the cylinder is presented in Fig. 5b.

Using the formula $p = \ln\left((L_2^{i+1} - L_2^i)/(L_2^i - L_2^{i-1})\right)/\ln(r)$ and a constant grid refinement ratio $r = 2$, the apparent order of convergence is $p = 1.992$ for the CLBM, $p = 1.986$ for the IDF-CLBM between the refining region ($D = 20 - 80$) and $p = 1.958$ for the IDF-CLBM between the refining region ($D = 10 - 40$). The superscripts in the L_2 terms denote the refinement levels. It is shown that the global second order accuracy of the CLBM is not significantly affected by the IBM. For the same test case, Wu and Shu [30] reported a convergence rate of 1.9 and Kang and Hassan [38] a convergence rate of 1.98. As pointed out by Zhang et al. [32], the use of the Lagrange interpolation formula, unlike the Dirac delta function, does not

Please cite this article in press as: E.J. Falagkaris, et al., PROTEUS: A coupled iterative force-correction immersed-boundary multi-domain cascaded lattice Boltzmann solver, Computers and Mathematics with Applications (2017), http://dx.doi.org/10.1016/j.camwa.2017.07.016.

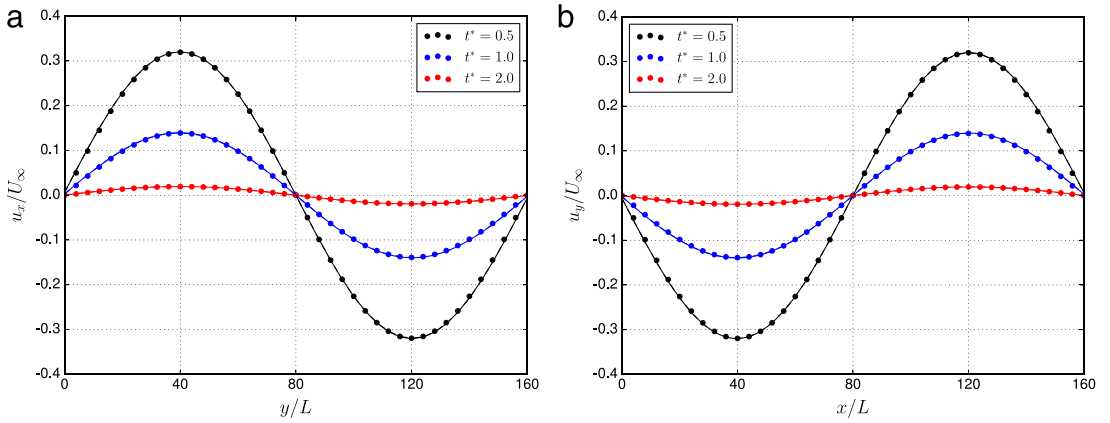

Fig. 6. Comparison of (a) the u_x velocity component at $x = L/2$ and (b) the u_y velocity component at $y = L/2$ in a decaying Taylor–Green vortex flow for $Re = 10$ at three non-dimensional times $t^* = 0.5, 1.0, 2.0$. The analytical values are plotted with dots and the computational values of the CLBM and the IDF-CLBM are plotted with continuous and dashed lines respectively.

introduce similar numerical velocity slip at the fluid nodes near the boundary and improves the local accuracy of the method. The reader should refer to Geller et al. [52] for an interesting discussion on the computational efficiency and accuracy of the LBM. The computed velocities of both the CLBM and the IDF-CLBM at three non-dimensional times are plotted in Fig. 6. Good agreement between the computed and the analytical values is observed.

3.2. Flow over a circular cylinder

The first validation example is the simulation of flows past a circular cylinder. In this extensively studied, both numerically and experimentally, problem, the flow behavior changes according to the Reynolds number, which is defined as $Re = u_\infty D/\nu$. D is the diameter of the cylinder, u_∞ is the freestream velocity and ν is the kinematic viscosity. In order to avoid the transition range, $Re = 150-300$, of the flow to 3D [53,54], $Re = 20$, 40, 100 and 150 are examined. In the present method, the external forces can be computed directly from the boundary forces obtained from the IDF scheme. For the lift force, the spanwise component $F_{l,y}$, of the boundary force is used

$$F_L = -\sum_l F_{l,y}\Delta s_l, \tag{31}$$

whereas the streamwise component $F_{l,x}$ of the boundary force is used for the computation of the drag force.

$$F_D = -\sum_l F_{l,x}\Delta s_l. \tag{32}$$

The summation is performed over all Lagrangian points. Δs_l is the discretization length of the immersed surface and should be equal for all points l. Unless otherwise specified, the forcing point is uniformly distributed with $\Delta s_l = 1.0$. Using Eqs. (31)–(32), the lift and drag coefficients are defined as

$$C_l = \frac{F_L}{0.5\rho U_\infty^2 D}, \tag{33}$$

$$C_d = \frac{F_D}{0.5\rho U_\infty^2 D}. \tag{34}$$

The initial density is taken as $\rho = 1.0$. At $Re = 20$ and $Re = 40$ the freestream velocity is set to $U_\infty = 0.1$ and to $U_\infty = 0.04$ at $Re = 100$ and $Re = 150$ respectively. The computational domain is $50D \times 50D$ with nine levels of grid refinement. The region around the cylinder is $4D \times 2D$ with a uniform mesh of 405×205 grid points.

3.2.1. Steady flow over a circular cylinder

For $Re = 20$ and 40, a development of two symmetric, stationary recirculating eddies is observed behind the cylinder. The wake length L_w or, recirculation length, is defined as $L_w = 2L/D$ where, L is the distance from the rearmost point of the cylinder to the end of the wake, as shown in Fig. 7. The separation angle θ_s is defined as the angle between the rearmost point of the cylinder and the point s on the cylinder surface where the shear stress is zero. The drag coefficient C_d, the wake length L_w and the separation angle θ_s are compared with other numerical and experimental results [30,55–58] in Table 1. Both immersed boundary treatments agree well with the other results in the literature.

Please cite this article in press as: E.J. Falagkaris, et al., PROTEUS: A coupled iterative force-correction immersed-boundary multi-domain cascaded lattice Boltzmann solver, Computers and Mathematics with Applications (2017), http://dx.doi.org/10.1016/j.camwa.2017.07.016.

Table 1
Comparison of Drag coefficient, wake length L_w and separation angle θ_s for steady flow over a circular cylinder at $Re = 20$ and 40.

Case	References	C_d	L_w	θ_r (deg)
$Re = 20$	Dennis and Chang [55]—Finite difference, NSE	2.045	1.88	43.7
	Fornberg [56]—Body-fitted grid, NSE	2.000	1.82	–
	He and Doolen [57]—Interpolation-supplemented, LBM	2.152	1.842	42.96
	Wu and Shu [30]—Implicit velocity correction IBM, LBM	2.091	1.86	–
	Nieuwstadt and Keller [58]—Vorticity streamfunction, NSE	2.053	1.786	43.37
	Present—IDF-CLBM	2.019	1.857	43.06
	Present—MDF-CLBM	2.005	1.882	43.45
$Re = 40$	Dennis and Chang [55]—Finite difference, NSE	1.522	4.69	53.8
	Fornberg [56]—Body-fitted grid, NSE	1.498	4.48	–
	He and Doolen [57]—Interpolation-supplemented, LBM	1.499	4.49	52.84
	Wu and Shu [30]—Implicit velocity correction, IBM	1.565	4.62	–
	Nieuwstadt and Keller [58]—Vorticity streamfunction, NSE	1.550	4.357	53.34
	Present—IDF-CLBM	1.524	4.61	53.12
	Present—MDF-CLBM	1.522	4.567	53.41

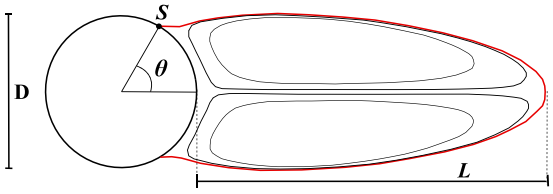

Fig. 7. Wake length L and separation angle θ_s for steady flow over a circular cylinder.

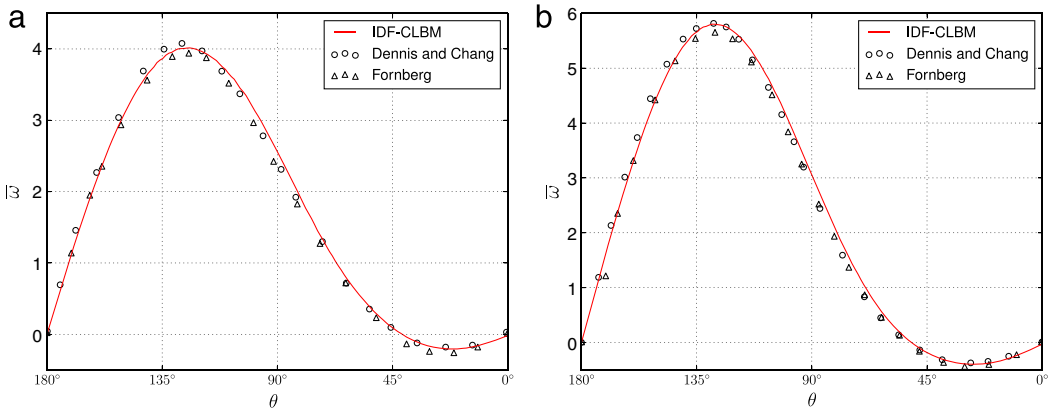

Fig. 8. Physical vorticity distribution on the surface of the cylinder at (a) $Re = 20$ and (b) $Re = 40$.

The physical vorticity $\overline{\omega}$, around the surface of the cylinder at $Re = 20$ and $Re = 40$ is compared with the results of Fornberg [56] and Dennis [55] in Fig. 8. All dimensionless quantities in the LBM can be converted into physical quantities as $\overline{\chi} = \chi C_\chi$, where C_χ is a conversion factor and χ is the dimensionless quantity. Therefore, $\overline{\omega}$ can be computed as

$$\overline{\omega} = \omega C_\omega = \frac{\omega}{C_t} = \frac{\omega \overline{u}}{u C_L^2}, \tag{35}$$

where C_ω, C_t and C_L are the conversion factors for the vorticity, the time and the characteristic length of the physical problem respectively.

3.3. Computational efficiency and iteration convergence rate

The relative computational effort of the bulk flow (CLBM), the immersed boundary method and the main steps in the IBM are presented in Table 2, based on two runs on each of three different architectures. In all cases the relative efforts are the same. The computational grid consists of 10^6 points and the immersed body is discretized using 312 points. $N = 20$ iterations are used in both immersed boundary methods. The two additional steps in the IDF scheme increase its computational cost

Please cite this article in press as: E.J. Falagkaris, et al., PROTEUS: A coupled iterative force-correction immersed-boundary multi-domain cascaded lattice Boltzmann solver, Computers and Mathematics with Applications (2017), http://dx.doi.org/10.1016/j.camwa.2017.07.016.

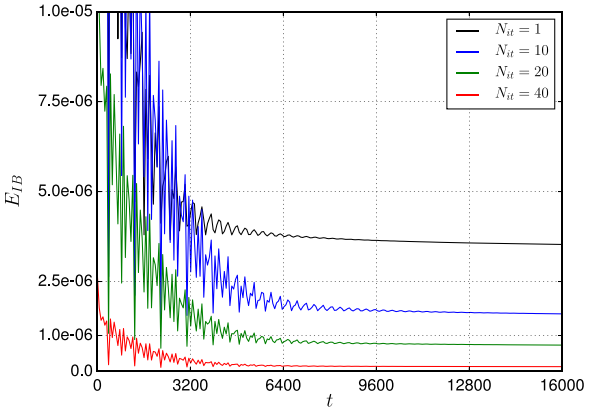

Fig. 9. Iteration convergence rate of the average boundary error E_{IB} at different numbers of iterations for the flow around the circular cylinder at $Re = 40$. The average boundary error E_{IB} is computed using Eq. (30), where the summation is taken over all Lagrangian points.

Table 2
Computational time percentages of the bulk flow (CLBM), the immersed boundary method and the main IBM steps shown in Fig. 2.

	CLBM (%)	IBM (%)	Velocity—int (%)	Force spreading (%)	Discrete force (%)	Streaming (%)
IDF-CLBM	93.6	6.40	0.95	2.46	1.17	0.47
MDF-CLBM	95.4	4.61	0.93	2.41	–	–

Table 3
Comparison of lift coefficient, drag coefficients and Strouhal number for unsteady flow over a circular cylinder at $Re = 100$.

Case	References	$Avg.C_d$	C_l	St
$Re = 100$	Williamson [59]—Experiment	–	–	0.166
	Lai and Peskin [60]—2nd order IBM-NSE	1.447	±0.330	0.165
	Liu et al. [61]—Body-fitted method, NSE	1.35	±0.339	0.164
	Wu and Shu [30]—Implicit velocity correction IBM, LBM	1.364	±0.344	0.163
	Choi et al. [62]—Higher order IBM-NSE	1.34	±0.315	0.164
	Kang and Hassan [38]—Exterior sharp direct forcing, LBM	1.336	±0.329	0.165
	Present IDF-CLBM	1.334	±0.331	0.165
	Present MDF-CLBM	1.330	±0.327	0.164

over the MDF scheme by 32.8%. However, since both steps have an influence range close to the boundary and are not related to the number of IB points, the computational cost would not increase if a finer representation of the boundary was selected. The overall computational overhead of the IDF-CLBM over the MDF-CLBM is limited to 2.1%. As a final remark, increasing the number of iterations in the IFD scheme from $N = 1$ to $N = 20$ leads to a 6.4% increase in the overall computational cost. However, as shown in Fig. 9, that increase in N significantly reduces the boundary error by an order of magnitude. It should be noted that the errors shown in Fig. 9 are case specific and are not representative of all the cases presented in this study.

3.3.1. *Unsteady flow over a circular cylinder*

For $Re = 100$ and 150, vortices are shed from the body. The Strouhal number is defined as

$$St = \frac{f_d D}{U_\infty}, \tag{36}$$

where f_d is the shedding frequency. Tables 3 and 4 present average drag coefficients, minimum and maximum values of lift coefficients and Strouhal numbers. The results are compared with other numerical schemes and experiments [30,38,59–62]. Both methods are in good agreement with the literature. Fig. 10 shows the time evolution of the lift and drag coefficients for the IDF-CLBM and the MDF-CLBM. The MDF-CMLB computed a slightly lower drag coefficient than the IDF-CLBM. The relative time t^* is defined as $t^* = t^n U_\infty / D$, where t^n is the current timestep.

At $Re = 150$, the IDF-CLBM drag coefficient has a better agreement with the body-fitted method of Liu et al. [61] with a relative error $<1\%$. Overall, the no-slip boundary condition on the immersed surface is well satisfied and a momentum exchange between the interior and the exterior to the boundary fluid domains, that would increase the computed force is minimized.

The time averaged physical vorticity $\overline{\omega^*}$, around the surface of the cylinder at $Re = 100$ is compared with the results of Fornberg [56] and Dennis and Chang [55] in Fig. 11. The present IDF-CLMB agrees well with the body-fitted method of Fornberg [56] and the finite difference solver of Dennis and Chang [55].

Please cite this article in press as: E.J. Falagkaris, et al., PROTEUS: A coupled iterative force-correction immersed-boundary multi-domain cascaded lattice Boltzmann solver, Computers and Mathematics with Applications (2017), http://dx.doi.org/10.1016/j.camwa.2017.07.016.

Table 4
Comparison of lift coefficient, drag coefficients and Strouhal number for unsteady flow over a circular cylinder at $Re = 150$.

Case	References	$Avg.C_d$	C_l	St
$Re = 150$	Williamson [59]—Experiment	–	–	0.183
	Lai and Peskin [60]—2nd order IBM-NSE	1.44	–	0.184
	Liu et al. [61]—Body-fitted method, NSE	1.334	±0.530	0.182
	Kang and Hassan [38]—Exterior sharp direct forcing, LBM	1.312	±0.513	0.184
	Present IDF-CLBM	1.327	±0.528	0.182
	Present MDF-CLBM	1.322	±0.522	0.183

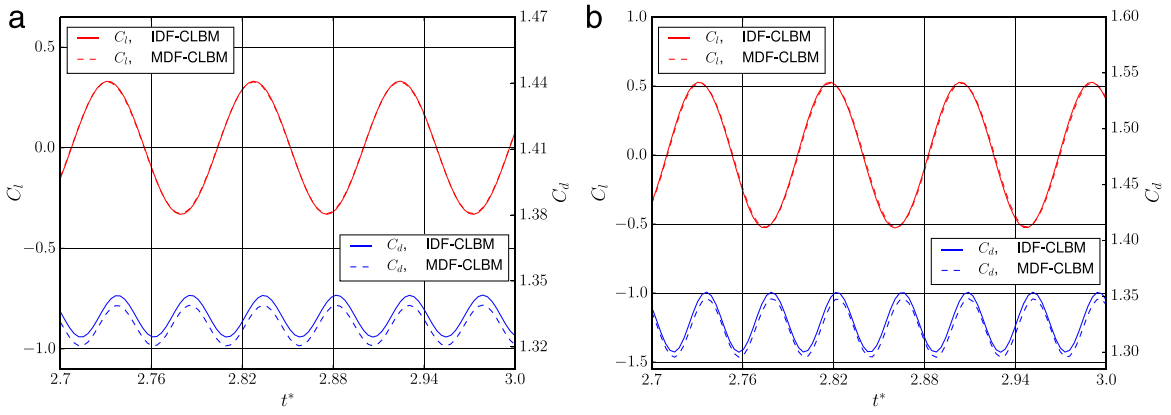

Fig. 10. Time evolution of lift and drag coefficients for the flow around a circular cylinder at (a) $Re = 100$ and (b) $Re = 150$.

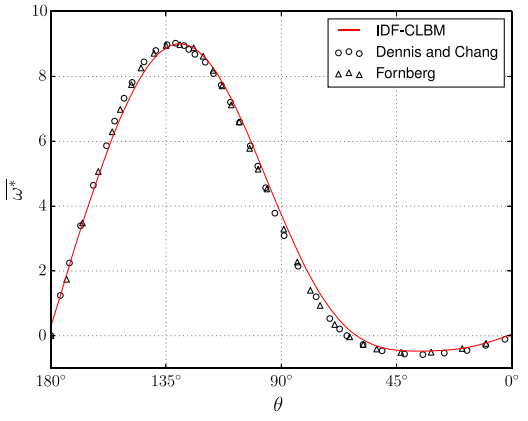

Fig. 11. Time averaged physical vorticity distribution on the surface of the cylinder at $Re = 100$.

3.4. Flow over a NACA-0012 airfoil

The flow around a NACA-0012 airfoil is investigated in this section. Because of the streamlined shape of the airfoil, a body-fitted method would be a usual approach in order to get high accuracy in the aerodynamic coefficients. This issue is addressed by further refining the region around the airfoil, while maintaining a uniform Cartesian grid. The computational domain is $100c \times 100c$ [63], where $c = 400\delta x$ is the chord of the airfoil and $\delta x = 1.0$ is the uniform grid spacing. Ten levels of grid refinement are used in order to ensure that the boundaries will not deteriorate the accuracy of the solution. The region around the airfoil is $1.5c \times 0.5c$ with a uniform mesh of 605×205 grid points.

Four different test cases are studied for the flow around the NACA-0012 airfoil as shown in Table 5. Similar to the flow around the circular cylinder, the density is initialized with $\rho = 1.0$. In Table 5, N_{iter} is the number of iteration in the IDF scheme.

Please cite this article in press as: E.J. Falagkaris, et al., PROTEUS: A coupled iterative force-correction immersed-boundary multi-domain cascaded lattice Boltzmann solver, Computers and Mathematics with Applications (2017), http://dx.doi.org/10.1016/j.camwa.2017.07.016.

Table 5
Test cases for the NACA-0012 airfoil.

Case	Re	AoA (deg)	c (δx)	U_∞	Wake	N_{iter}
1	500	0	400	0.1	Steady	20
2	1 000	10	400	0.04	Unsteady	20
3	5 000	10	400	0.02	Unsteady	40
4	100 000	10	800	0.01	Unsteady	80

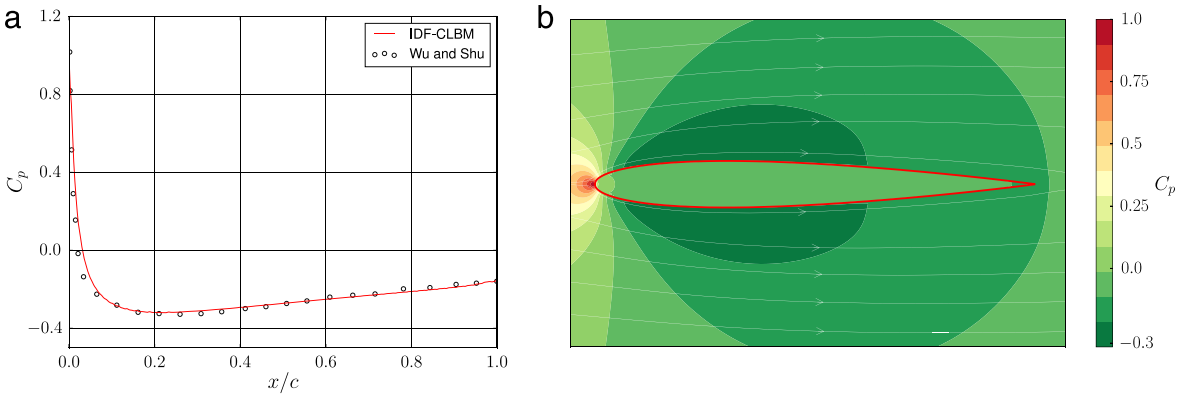

Fig. 12. (a) Comparison of the pressure coefficient C_p distribution along the NACA-0012 airfoil at $Re = 500$ and $AoA = 0°$. (b) Streamlines and pressure coefficient contour for the flow around the NACA-0012 airfoil at $Re = 500$ and $AoA = 0°$.

3.4.1. Steady flow over a NACA-0012 airfoil

The first test case studies the steady flow around the NACA-0012 airfoil at $Re = 500$ at $AoA = 0°$. The time averaged pressure coefficient can be computed as

$$C_p = \frac{p(\mathbf{X}_l) - p_\infty}{0.5\rho U_\infty^2}, \tag{37}$$

where p_∞ is the freestream pressure. The pressure $p(\mathbf{X}_l)$ on the surface of the airfoil can be interpolated from the surrounding fluid nodes. In the present study, only the exterior to the boundary fluid nodes is used in the interpolation. The distribution of the pressure coefficient along the surface of the airfoil and the pressure contours along with the streamlines are presented in Fig. 12. The results are in very good agreement with the implicit velocity correction-based method of Wu and Shu [30].

Fig. 13 indicates the boundary layer velocity profile at different positions with respect to the chord of the airfoil ($x/c = 0.0, 0.25, 0.5, 0.75, 1.0$).

The time averaged velocity profile over 20 000 time-steps at a steady state flow is used. The results are in good proximity with the ones reported by Imamura et al. [64] using a LBM on a generalized coordinate system.

The boundary layer thickness δ, as well as the displacement thickness δ_1 and the momentum thickness δ_2, are also computed and compared with the Blasius solution for a flat plate at the same Re, as shown in Fig. 14. The boundary layer thickness δ is computed using the vorticity decay criterion. As shown in Fig. 15, the vorticity ω outside the edge of the boundary layer (red line) is negligible and the flow is almost irrotational with $\nabla \times \mathbf{u} = 0$. The computational procedure used in the present study is as follows. First, the vorticity is interpolated on the wall normal directions $\mathbf{n}_l$ for each Lagrangian marker l on the immersed body. The maximum value of the vorticity $(\omega)_{\mathbf{n}_l}$ for each $\mathbf{n}_l$ is stored. Finally, δ is defined as the distance from the wall where $\omega_{\mathbf{n}_l}$ has decayed to a small fraction of the maximum vorticity $(\omega)_{\mathbf{n}_l}$ near the wall

$$\hat{\omega}_{\mathbf{n}_l} = \frac{\omega_{\mathbf{n}_l}}{(\omega)_{\mathbf{n}_l}} \leq \epsilon, \tag{38}$$

where $\epsilon = 0.02$ is chosen based on the flat plate correlation. Knowing δ, the displacement thickness δ_1 and the momentum thickness δ_2 are computed as

$$\delta_1 = \int_0^\delta \left(1 - \frac{u_{\mathbf{n}_l}}{U_{\mathbf{n}_l,\delta}}\right) dy, \qquad \delta_2 = \int_0^\delta \frac{u_{\mathbf{n}_l}}{U_{\mathbf{n}_l,\delta}} \left(1 - \frac{u_{\mathbf{n}_l}}{U_{\mathbf{n}_l,\delta}}\right) dy, \tag{39}$$

where $u_{\mathbf{n}_l}$ and $U_{\mathbf{n}_l,\delta}$ are the tangential components of the computed velocity and the outer velocity on the normal to the wall directions $\mathbf{n}_l$.

Fig. 14a shows that the accelerated flow from the leading edge leads in a thinner boundary layer than the flat plate. However, at about 90% of the chord, the boundary layer has fully recovered its thickness due to the adverse pressure gradient. In Fig. 14b, a similar behavior is observed for the momentum thickness, δ_2. The displacement thickness recovers at approximately 55% of the chord length.

Please cite this article in press as: E.J. Falagkaris, et al., PROTEUS: A coupled iterative force-correction immersed-boundary multi-domain cascaded lattice Boltzmann solver, Computers and Mathematics with Applications (2017), http://dx.doi.org/10.1016/j.camwa.2017.07.016.

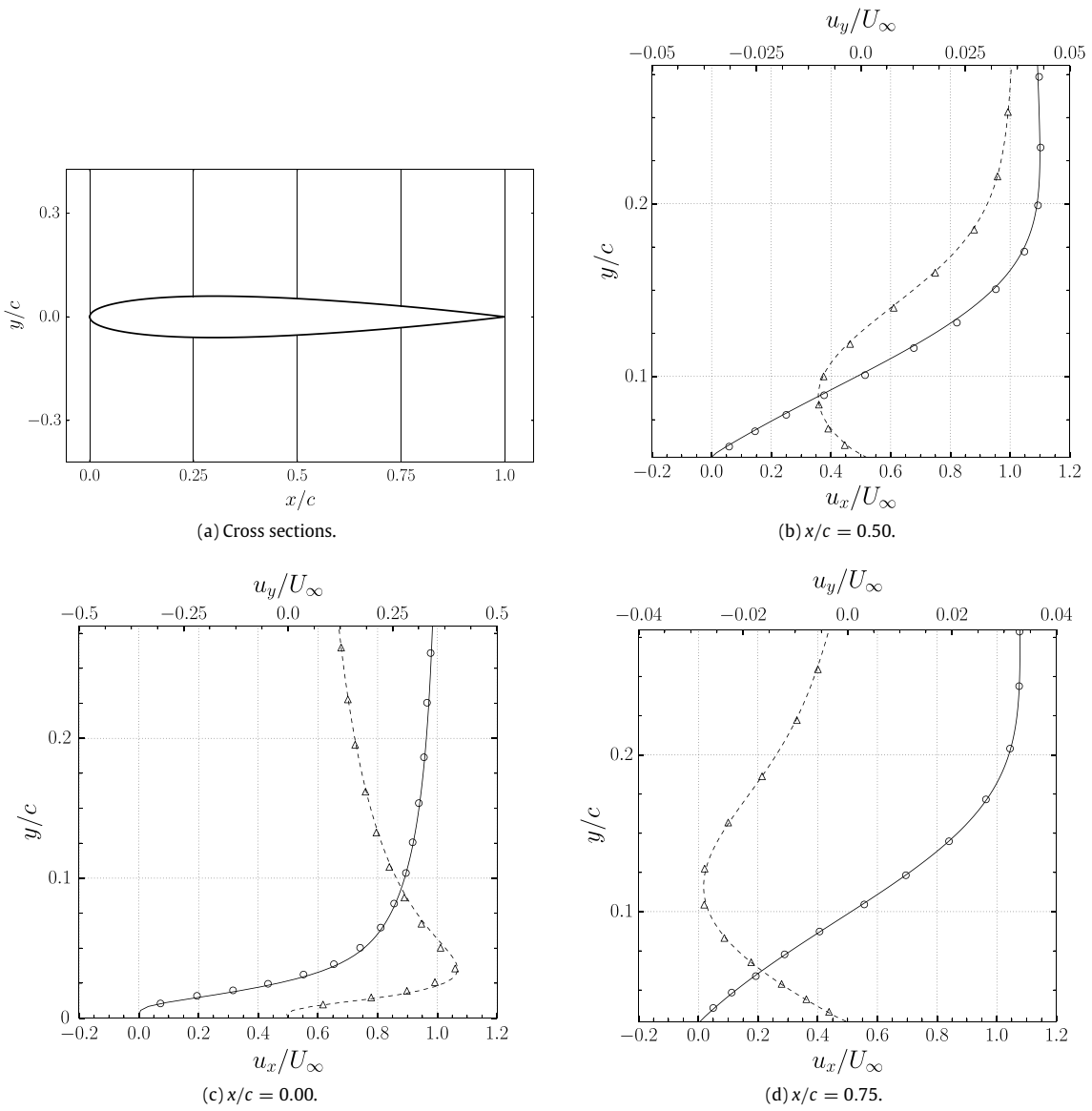

Fig. 13. Comparison of the time averaged velocity profile of NACA 0012 at various cross sections x/c. The normal and dashed lines are the u_x/U_∞ and u_y/U_∞ respectively, of the IDF-CLBM. The results from Imamura [64] are plotted with circles and triangles.

3.4.2. Unsteady flow over a NACA-0012 airfoil

At $Re = 1000$ and $AoA = 10°$, the computed Strouhal number is 0.861, which compares well with the value of 0.862 reported by Mittal and Tezduyar [63] and the value of 0.86 reported by Johnson and Tezduyar [65]. Fig. 16a, shows the time evolution of the lift and drag coefficients. The time averaged, over the last four periods, lift coefficient is compared with the reported values in [63] and [65] as shown in Fig. 16b. Our results agree well with the ones reported in [65]. Mittal and Tezduyar [63] reported a 2% higher value of the lift coefficient.

Fig. 17 shows the boundary layer thickness around the NACA-0012 airfoil. The time averaged vorticity over ten oscillation periods is used.

At $Re = 5000$ and $AoA = 10°$, the presence of stronger vortices on the surface of the airfoil result in higher average values of the aerodynamic coefficients. Fig. 18a shows the time evolution of the lift and drag coefficients. In order to accurately capture the flow characteristics, a lattice freestream velocity $U_\infty = 0.02$ is used. The magnitudes of the temporarily fluctuating components of the aerodynamic coefficients are also higher for $Re = 5000$. The lift coefficient computed with the IDF-CLBM agrees well with the one reported in [63], as shown in Fig. 18b. At both $Re = 1000$ and $Re = 5000$, the magnitude of oscillation of the lift coefficient reported in [63] is slightly lower than the one computed with IDF-CLBM.

Please cite this article in press as: E.J. Falagkaris, et al., PROTEUS: A coupled iterative force-correction immersed-boundary multi-domain cascaded lattice Boltzmann solver, Computers and Mathematics with Applications (2017), http://dx.doi.org/10.1016/j.camwa.2017.07.016.

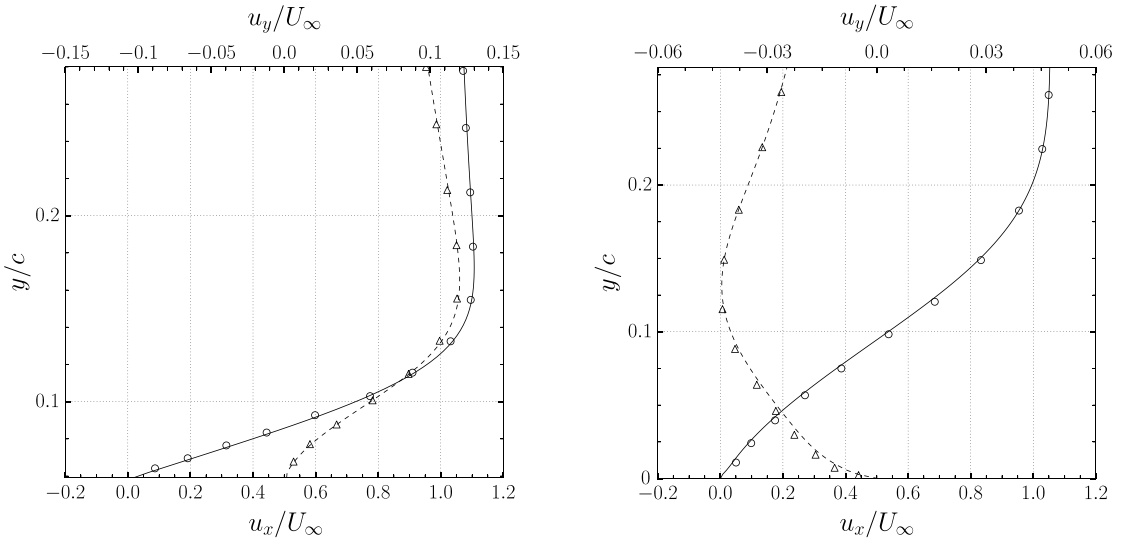

(e) $x/c = 0.25$. (f) $x/c = 1.00$.

Fig. 13. (*continued*)

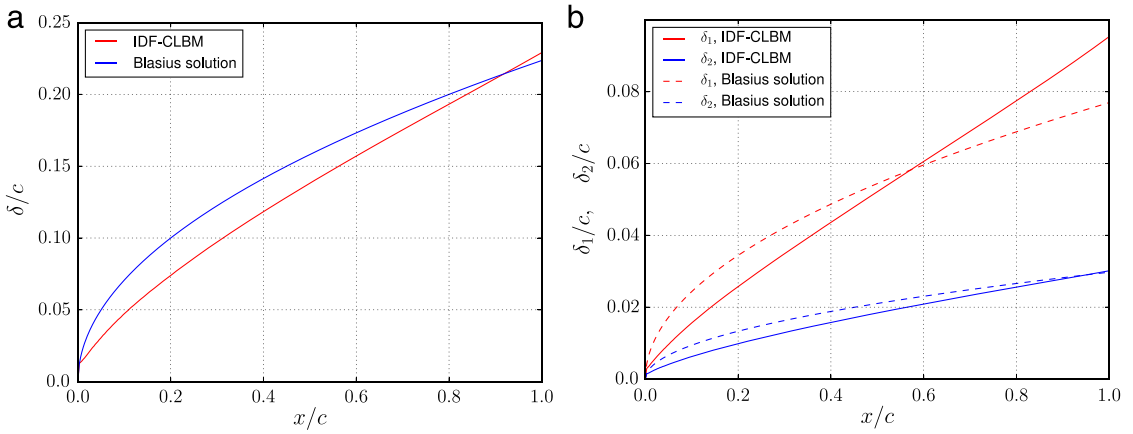

Fig. 14. (a) Boundary layer thickness with Blasius solution (b) Displacement (δ_1) and momentum (δ_2) thickness with Blasius solution.

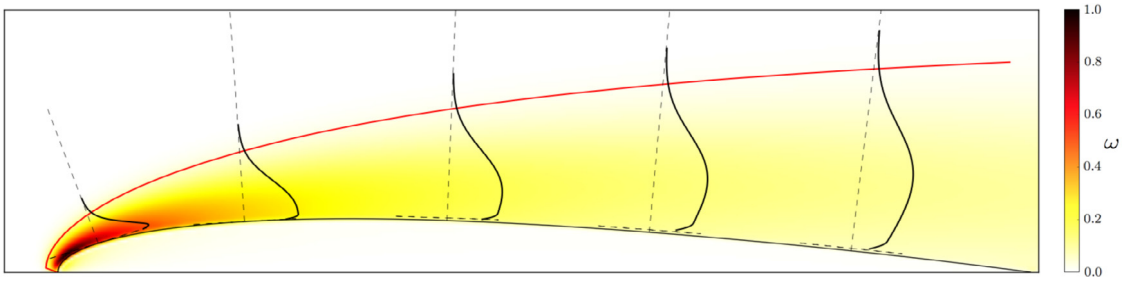

Fig. 15. Normalized absolute vorticity field around the NACA-0012 at $Re = 500$ and boundary layer thickness δ (red line). The black lines show the vorticity $\omega_{\mathbf{n}_l}$, scaled with the maximum value $(\omega)_{\mathbf{n}_l}$, on the normal directions $\mathbf{n}_l$. (For interpretation of the references to color in this figure legend, the reader is referred to the web version of this article.)

Please cite this article in press as: E.J. Falagkaris, et al., PROTEUS: A coupled iterative force-correction immersed-boundary multi-domain cascaded lattice Boltzmann solver, Computers and Mathematics with Applications (2017), http://dx.doi.org/10.1016/j.camwa.2017.07.016.

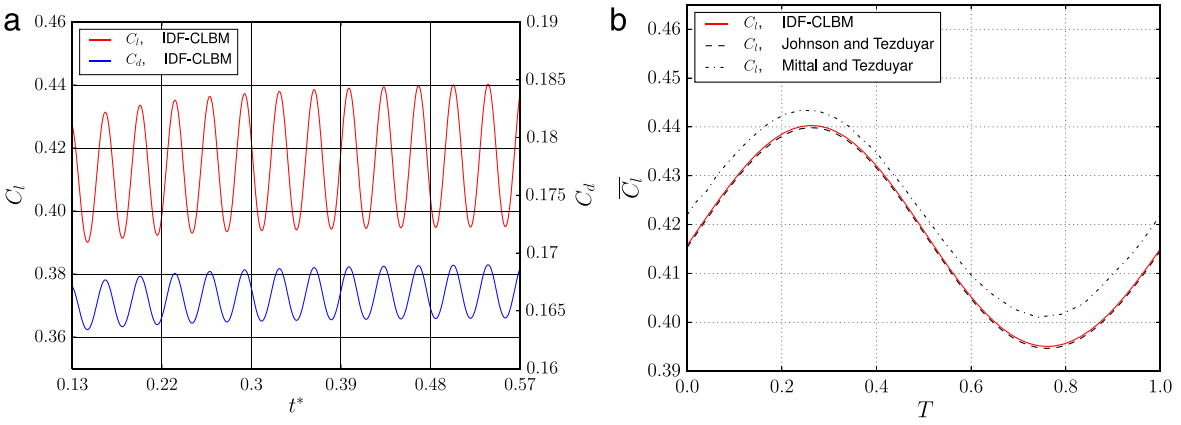

Fig. 16. (a) Time evolution of lift and drag coefficients for the flow around a NACA-0012 airfoil at $Re = 1000$ and $AoA = 10°$, (b) Averaged lift coefficient $\overline{C_l}$, over four oscillations with period T.

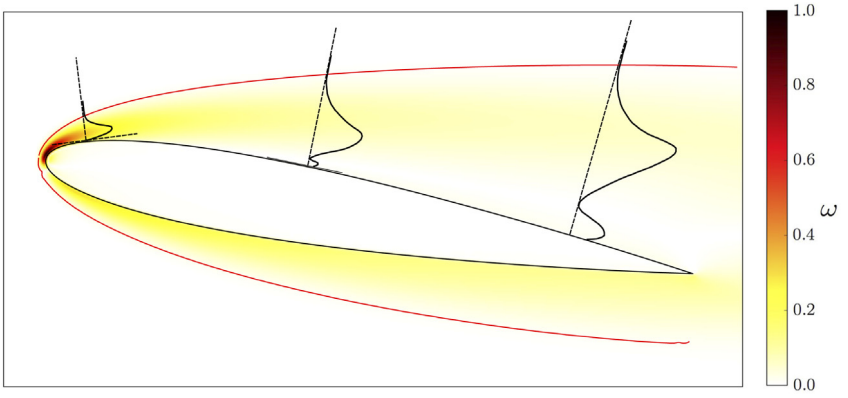

Fig. 17. Normalized absolute vorticity field around the NACA-0012 at $Re = 1000$ and boundary layer thickness δ (red line). The black lines show the vorticity $\omega_{\mathbf{n}_l}$, scaled with the maximum value $(\omega)_{\mathbf{n}_l}$, on the normal directions $\mathbf{n}_l$. (For interpretation of the references to color in this figure legend, the reader is referred to the web version of this article.)

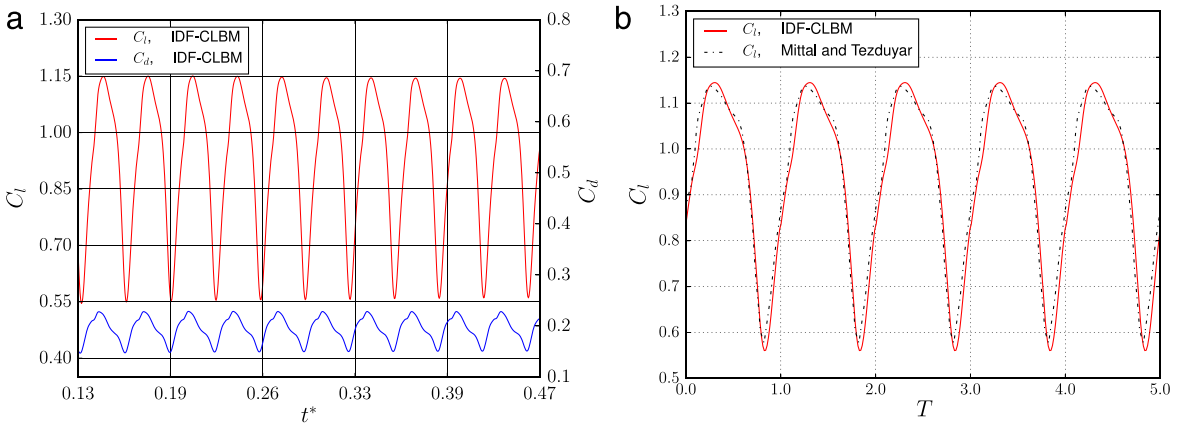

Fig. 18. (a) Time evolution of lift and drag coefficients for the flow around a NACA-0012 airfoil at $Re = 5000$ and $AoA = 10°$, (b) Lift coefficient over five oscillation periods.

Fig. 20 shows a sequence of frames for the instantaneous vorticity around the airfoil during one period of the lift coefficient. The first frame 20a corresponds to the minimum lift coefficient, whereas the fourth frame 20d corresponds to the maximum lift coefficient. It is noticed that the interaction between the vortices shed from the upper and the lower

Please cite this article in press as: E.J. Falagkaris, et al., PROTEUS: A coupled iterative force-correction immersed-boundary multi-domain cascaded lattice Boltzmann solver, Computers and Mathematics with Applications (2017), http://dx.doi.org/10.1016/j.camwa.2017.07.016.

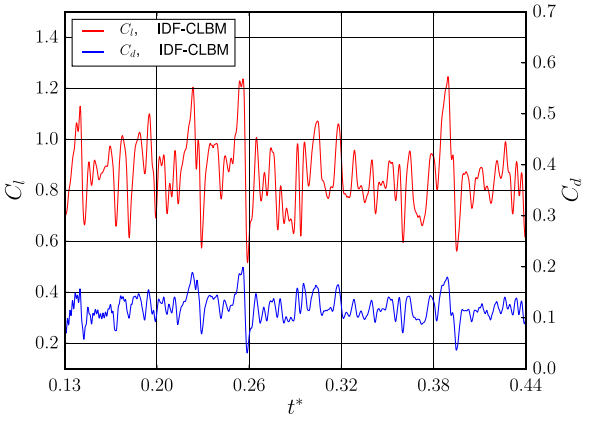

Fig. 19. Time evolution of lift and drag coefficients for the flow around a NACA-0012 airfoil at $Re = 10^5$ and $AoA = 10°$.

Table 6
Statistics for the time evolution of the lift and drag coefficients for the flow around a NACA-0012 airfoil at $Re = 10^5$ and $AoA = 10°$.

	Reference	Mean	St. deviation	Min	Max
C_L	Mittal and Tezduyar [63]	0.82705	0.15917	0.30035	1.24603
	Present IDF-CLBM	0.85577	0.12797	0.51671	1.24583
C_D	Mittal and Tezduyar [63]	0.11457	0.02995	0.03149	0.19888
	Present IDF-CLBM	0.11724	0.02776	0.03139	0.20724

surfaces of the airfoil generates an upwards moving wake with counter-rotating vortices. A similar conclusion is reported in [63]. The computed Strouhal number, based on the dominant frequency is 0.681 which agrees well with the value of 0.685 of Mittal and Tezduyar [63].

At $Re = 10^5$ and $AoA = 10°$, a direct comparison with other numerical simulations is not feasible. The freestream lattice velocity is set to $U_\infty = 0.01$ and the chord of the airfoil at $c = 800\delta x$ with $\delta x = 1.0$. Fig. 19 shows the time histories of the aerodynamic coefficients acting on the airfoil.

Table 6 summarizes some statistical characteristics of the time evolution of the lift and drag coefficients. The results are compared with the ones reported in Mittal and Tezduyar [63] and good agreement is observed on the drag coefficient. However, differences are observed in the lift coefficient. Although the mean and maximum values are closely related, a divergence is observed in the standard deviation and the minimum value. The quantile–quantile (Q–Q) plots in Fig. 21 compare the data of the lift and drag coefficients obtained with the IDF-CLBM with the data reported in Mittal and Tezduyar [63]. Good statistical proximity is observed for the drag coefficient with a 5% average divergence between the two data sets. However, as seen in Fig. 21a, below the mean value, the data range for the lift coefficient significantly diverges.

According to Mittal and Tezduyar [63], flows at such high Reynolds numbers are considered turbulent in nature. It should be noted that Case 4 could be considered as a limit to the current IDF immersed boundary algorithm. Although the no-slip boundary condition is still satisfied, the effect of the force spreading operation in the immersed boundary scheme and the first order of accuracy of the Dirac delta function distorts the accuracy of the solution around the immersed boundary. This leads to discontinuities of the velocity gradient on the boundary and decreases the order of accuracy of the solution. This can also be verified by the over-predicted values of the lift coefficient in Fig. 21a. This is a known issue of all immersed boundary treatments and further developments are necessary. As a final remark, the instantaneous vorticity at $t^* = 0.433, 0.436, 0.438, 0.44, 0.442, 0.444$ is shown in Fig. 22. It can be observed that separation of the flow on the upper surface of the airfoil occurs very close to the leading edge.

Case 4, demonstrates the robustness of our numerical scheme at high Reynolds number flows. In contrast to the previous cases, an unsteady motion of the internal fluid is observed at $Re = 10^5$, as shown in Fig. 22. The time derivative of the linear momentum of the internal fluid results in an internal force $\mathbf{F}^{int}$ given by:

$$\mathbf{F}^{int}(t) = \rho \frac{d}{dt} \int_{\mathbf{x} \in \Omega(t)} \mathbf{u}(\mathbf{x}, t) d\mathbf{x}. \tag{40}$$

The effect of the internal forces is more significant in moving boundary applications. However, in highly unsteady flow cases, compensating the internal forces in the computation of the aerodynamic forces should be further investigated.

4. Conclusions

A novel coupling between the CLBM and the IBM has been presented. To ensure stability and numerical accuracy, the central moment formulation of the LBM [17,18] has been chosen to solve the fluid dynamics equations. The iterative force

Please cite this article in press as: E.J. Falagkaris, et al., PROTEUS: A coupled iterative force-correction immersed-boundary multi-domain cascaded lattice Boltzmann solver, Computers and Mathematics with Applications (2017), http://dx.doi.org/10.1016/j.camwa.2017.07.016.

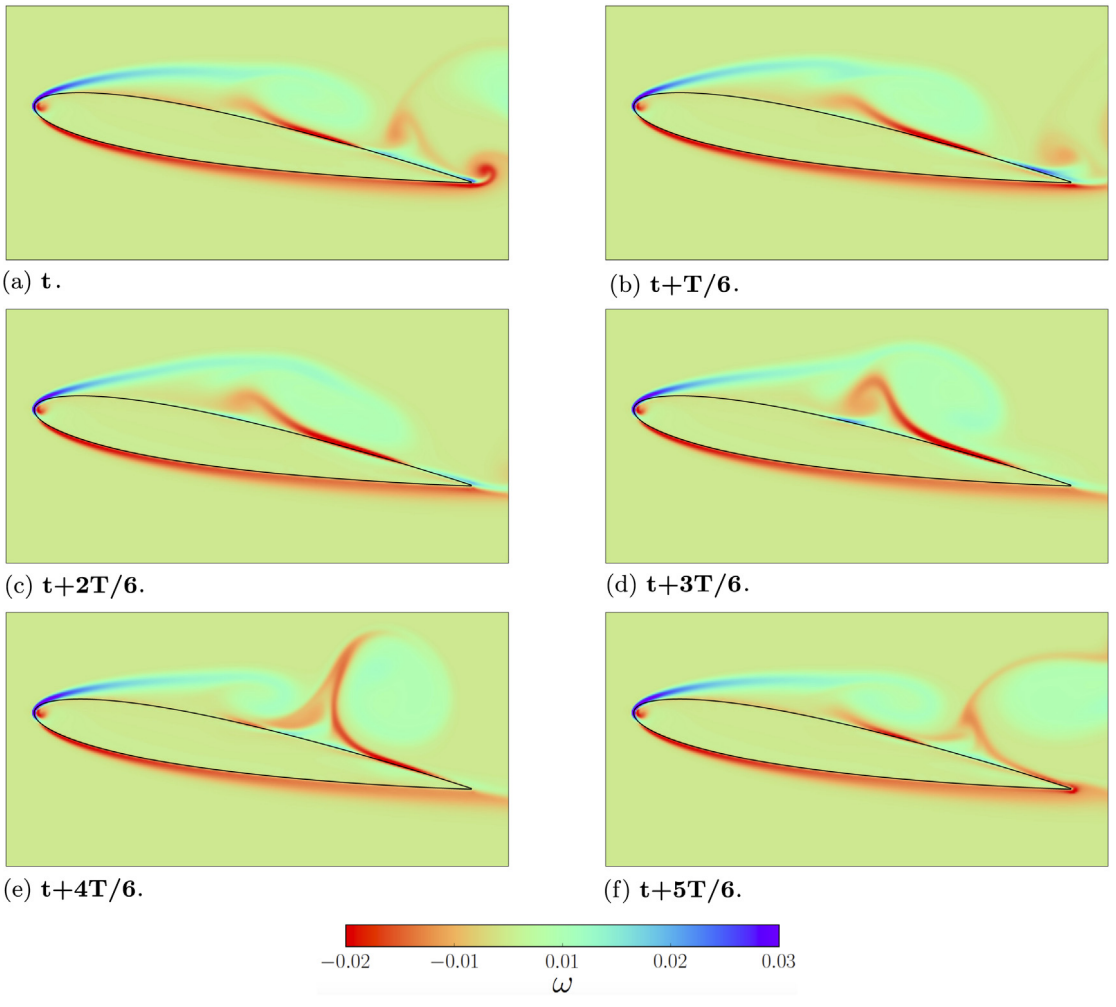

Fig. 20. Instantaneous vorticity around the NACA-0012 airfoil at $Re = 5000$ and $AoA = 10°$ for a period of oscillation of the lift coefficient.

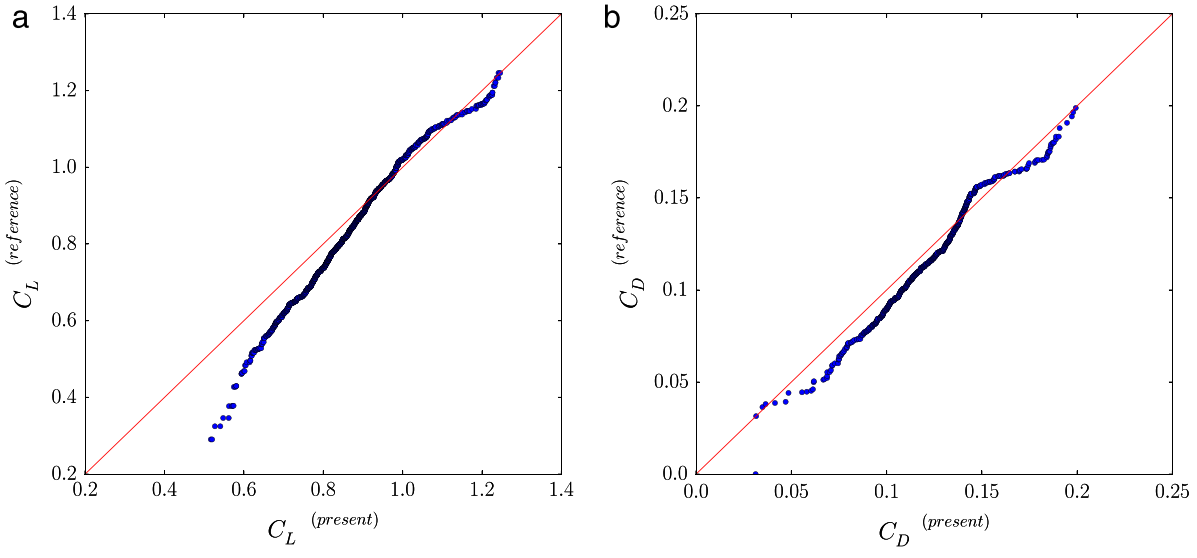

Fig. 21. (a) Q–Q plot for the lift coefficient, (b) Q–Q plot for the drag coefficient.

Please cite this article in press as: E.J. Falagkaris, et al., PROTEUS: A coupled iterative force-correction immersed-boundary multi-domain cascaded lattice Boltzmann solver, Computers and Mathematics with Applications (2017), http://dx.doi.org/10.1016/j.camwa.2017.07.016.

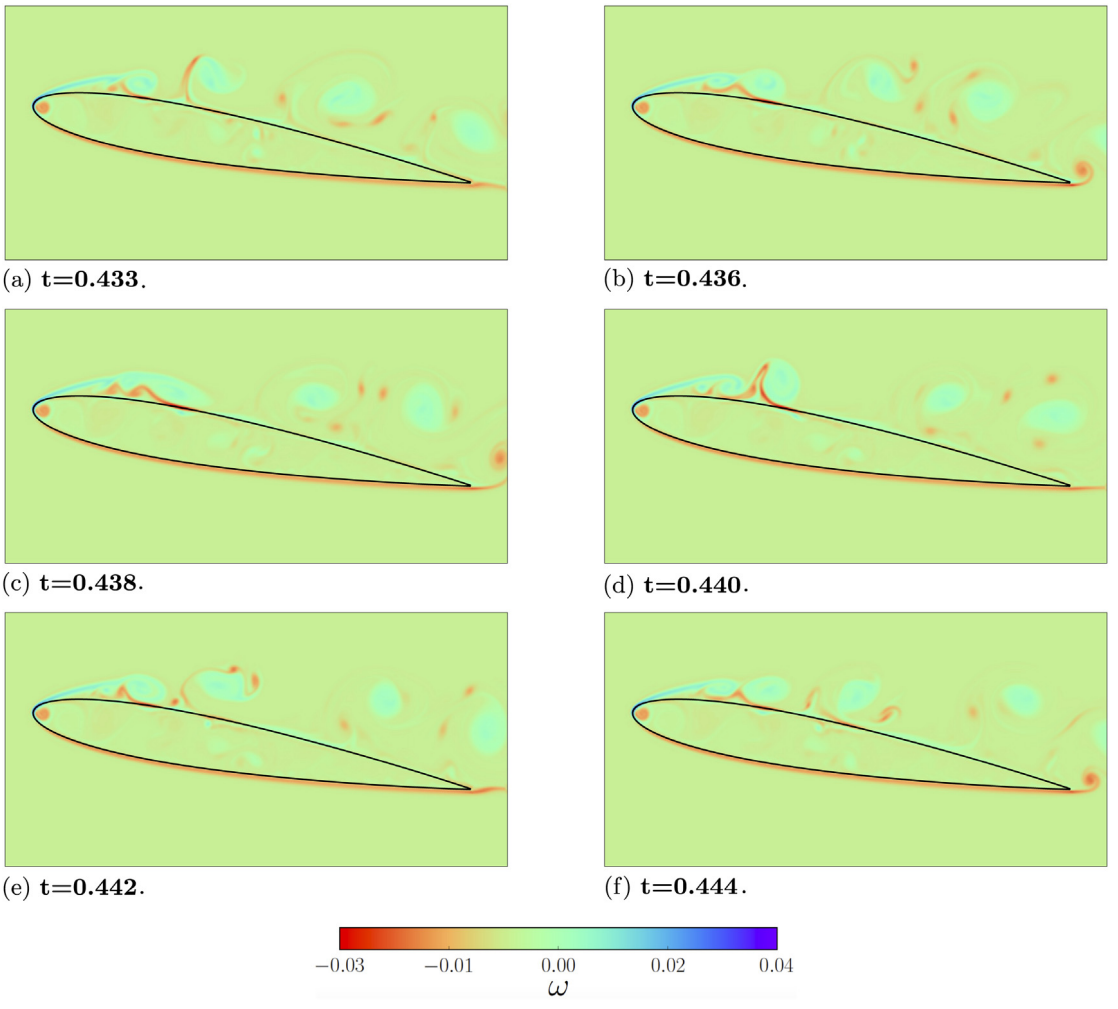

Fig. 22. Instantaneous vorticity around the NACA-0012 airfoil at $Re = 10^5$ and $AoA = 10^\circ$.

correction IBM recently proposed by Zhang et al. [32], has been coupled with the CLBM. The numerical accuracy of the boundary treatment has been enhanced by incorporating the effects of both the current and next time step in the discrete external forcing term. The proposed coupling scheme is found to be computationally efficient and geometrically flexible, indicating that the extension to moving boundaries may be tractable.

The robustness and numerical accuracy of the proposed scheme is demonstrated by studies of steady and unsteady flows around a circular cylinder and a NACA-0012 airfoil over a range of Reynolds numbers. The IDF is also compared with an established multi direct forcing IBM [38].

The study of the flow around a circular cylinder indicates that both the IDF and the MDF schemes are in good agreement with other numerical and experimental results in the literature. At Reynolds number of 100 and 150 (the limits for 2D flow), the results obtained with the present method are in better agreement with the results reported by Liu et al. [61], using a body-fitted NSE solver, than those from other IBM schemes presented in the literature. Four test cases are investigated for the flow around a NACA-0012 airfoil. At a low Reynolds of 500, the computed pressure coefficient and the boundary layer velocity profiles are in very good agreement with other numerical methods. The computed boundary layer thickness, Fig. 14, is identical to the analytical Blasius solution for a flat plate up to the point of maximum curvature on the airfoil surface. Beyond that point, as expected, the pressure gradient adversely affects the thickness of the boundary layer. The aerodynamic coefficients for the moderate Reynolds number cases (1000 and 5000) are accurately captured by the present scheme. The robustness of our scheme is demonstrated using a Reynolds number of 100 000. A statistical analysis of the time dependent solution indicates that the IDF-CLBM accurately reproduces the unsteady lift and drag behavior reported by Mittal and Tezduyar [63].

The present IDF-CLBM scheme has been shown to compute the aerodynamic coefficients and flow characteristics in the vicinity of an immersed body. In the majority of the cases, the present results compare well with body-fitted methods.

Please cite this article in press as: E.J. Falagkaris, et al., PROTEUS: A coupled iterative force-correction immersed-boundary multi-domain cascaded lattice Boltzmann solver, Computers and Mathematics with Applications (2017), http://dx.doi.org/10.1016/j.camwa.2017.07.016.

However, as the Reynolds number increases and the kinematic viscosity decreases, the effect of the use of the Dirac delta function in the force spreading operation (which is only first-order accurate) effectively decreases the numerical accuracy, giving rise to artificial numerical errors and leading to discontinuities in the velocity gradient at the boundary. This numerical dissipation cannot be resolved by further refining the computational grid, indicating that further developments of the method are necessary. Finally, the effect of the fluid forces inside the immersed boundary need further investigation.

Acknowledgments

The first author wishes to acknowledge funding from the Energy Technology Partnership (ETP) in support of his Ph.D. studies [ETP125]. The ETP is a pooling exercise funded by the Scottish Funding Council and Scottish Enterprise. The authors also wish to thank Dr. Timm Krüger for his advice.

References

[1] S. Chapman, T. Cowling, Mathematical Theory of Nonuniform Gases, Cambridge University Press, 1964.
[2] C. Cercignani, The Boltzmann Equation and Its Applications, in: Applied Mathematical Science, vol. 67, Springer, 1988.
[3] D.A. Wolf-Gladrow, Lattice-Gas Cellular Automata and Lattice Boltzmann Models: An Introduction, Springer, 2004.
[4] Y. Sone, Kinetic Theory and Fluid Dynamics, in: Modeling and Simulation in Science , Engineering and Technology, Springer, 2002.
[5] M. Junk, A. Klar, L.-S. Luo, Asymptotic analysis of the lattice Boltzmann equation, J. Comput. Phys. 210 (2) (2005) 676–704.
[6] P. Asinari, Generalized local equilibrium in the cascaded lattice Boltzmann method, Phys. Rev. E 78 (1) (2008).
[7] H. Grad, On the kinetic theory of rarefied gases, Comm. Pure Appl. Math. 2 (4) (1949) 331–407.
[8] M. Geier, A. Greiner, J.G. Korvink, A factorized central moment lattice Boltzmann method, Eur. Phys. J. Spec. Top. 171 (1) (2009) 55–61.
[9] H. Chen, S. Chen, W.H. Matthaeus, Recovery of the Navier-Stokes equations using a lattice-gas Boltzmann method, Phys. Rev. A 45 (8) (1992) R5339.
[10] Y.H. Qian, D. d'Humières, P. Lallemand, Lattice BGK models for Navier-Stokes equation, Europhys. Lett. 17 (6) (1992) 479.
[11] P.L. Bhatnagar, E.P. Gross, M. Krook, A Model for collision processes in gases. I. Small amplitude processes in charged and neutral one-component systems, Phys. Rev. 94 (3) (1954) 511.
[12] D. d'Humières, Generalized lattice-Boltzmann equations, in: Rarefied Gas Dynamics: Theory and Simulations, in: Progress in Astronautics and Aeronautics, vol. 159, American Institute of Aeronautics and Astronautics, 1992, pp. 450–458.
[13] I. Ginzburg, D. d'Humières, Multireflection boundary conditions for lattice Boltzmann models, Phys. Rev. E 68 (6) (2003).
[14] P.J. Dellar, Incompressible limits of lattice Boltzmann equations using multiple relaxation times, J. Comput. Phys. 190 (2) (2003) 351–370.
[15] S. Ansumali, I.V. Karlin, Single relaxation time model for entropic lattice Boltzmann methods, Phys. Rev. E 65 (5) (2002).
[16] S. Ansumali, I.V. Karlin, Stabilization of the lattice Boltzmann method by the H theorem: A numerical test, Phys. Rev. E 62 (2000) 7999–8003.
[17] M. Geier, Ab initio derivation of the cascaded Lattice Boltzmann Automaton, Ph.D. dissertation , University of Freiburg - IMTEK, 2006.
[18] M. Geier, A. Greiner, J.G. Korvink, Cascaded digital lattice Boltzmann automata for high Reynolds number flow, Phys. Rev. E 73 (6) (2006).
[19] M. Geier, M. Schönherr, A. Pasquali, M. Krafczyk, The cumulant lattice Boltzmann equation in three dimensions: Theory and validation, Comput. Math. Appl. 70 (4) (2015) 507–547.
[20] C.S. Peskin, Numerical analysis of blood flow in the heart, J. Comput. Phys. 25 (3) (1977) 220–252.
[21] C.S. Peskin, The immersed boundary method, Acta Numer. 11 (2002).
[22] R. Glowinski, T.W. Pan, T.I. Hesla, D.D. Joseph, J. Périaux, A fictitious domain approach to the direct numerical simulation of incompressible viscous flow past moving rigid bodies: Application to particulate flow, J. Comput. Phys. 169 (2) (2001) 363–426.
[23] K. Höfler, S. Schwarzer, Navier-Stokes simulation with constraint forces: Finite-difference method for particle-laden flows and complex geometries, Phys. Rev. E 61 (6) (2000) 7146.
[24] N.A. Patankar, P. Singh, D.D. Joseph, R. Glowinski, T.-W. Pan, A new formulation of the distributed Lagrange multiplier/fictitious domain method for particulate flows, Int. J. Multiph. Flow. 26 (9) (2000) 1509–1524.
[25] Z.-G. Feng, E.E. Michaelides, The immersed boundary-lattice Boltzmann method for solving fluid - particles interaction problems, J. Comput. Phys. 195 (2) (2004) 602–628.
[26] A. Dupuis, P. Chatelain, P. Koumoutsakos, An immersed boundary-lattice-Boltzmann method for the simulation of the flow past an impulsively started cylinder, J. Comput. Phys. 227 (9) (2008) 4486–4498.
[27] X.D. Niu, C. Shu, Y.T. Chew, Y. Peng, A momentum exchange-based immersed boundary-lattice Boltzmann method for simulating incompressible viscous flows, Phys. Lett. A 354 (3) (2006) 173–182.
[28] J. Zhang, P.C. Johnson, A.S. Popel, Red blood cell aggregation and dissociation in shear flows simulated by lattice Boltzmann method, J. Biomech. 41 (1) (2008) 47–55.
[29] Y. Cheng, H. Zhang, Immersed boundary method and lattice Boltzmann method coupled FSI simulation of mitral leaflet flow, Comput. Fluids 39 (5) (2010) 871–881.
[30] J. Wu, C. Shu, Implicit velocity correction-based immersed boundary-lattice Boltzmann method and its applications, J. Comput. Phys. 228 (6) (2009) 1963–1979.
[31] Z. Guo, C. Zheng, B. Shi, Discrete lattice effects on the forcing term in the lattice Boltzmann method, Phys. Rev. E 65 (4) (2002).
[32] C. Zhang, Y. Cheng, L. Zhu, J. Wu, Accuracy improvement of the immersed boundary-lattice Boltzmann coupling scheme by iterative force correction, Comput. Fluids 124 (2016) 246–260.
[33] K.N. Premnath, S. Banerjee, Incorporating forcing terms in cascaded lattice Boltzmann approach by method of central moments, Phys. Rev. E 80 (3) (2009) 036702.
[34] D. Yu, R. Mei, L.-S. Luo, W. Shyy, Viscous flow computations with the method of lattice Boltzmann equation, Prog. Aerosp. Sci. 39 (5) (2003) 329–367.
[35] Y. Cheng, J. Li, Introducing unsteady non-uniform source terms into the lattice Boltzmann model, Internat. J. Numer. Methods Fluids 56 (6) (2008) 629–641.
[36] X. Yang, X. Zhang, Z. Li, G.-W. He, A smoothing technique for discrete delta functions with application to immersed boundary method in moving boundary simulations, J. Comput. Phys. 228 (20) (2009) 7821–7836.
[37] Y. Cheng, L. Zhu, C. Zhang, Numerical study of stability and accuracy of the immersed boundary method coupled to the lattice Boltzmann BGK model, Commun. Comput. Phys. 16 (01) (2014) 136–168.
[38] S.K. Kang, Y.A. Hassan, A comparative study of direct-forcing immersed boundary-lattice Boltzmann methods for stationary complex boundaries, Internat. J. Numer. Methods Fluids 66 (9) (2011) 1132–1158.
[39] T. Inamuro, Lattice Boltzmann methods for moving boundary flows, Fluid Dynam. Res. 44 (2) (2012) 024001.

Please cite this article in press as: E.J. Falagkaris, et al., PROTEUS: A coupled iterative force-correction immersed-boundary multi-domain cascaded lattice Boltzmann solver, Computers and Mathematics with Applications (2017), http://dx.doi.org/10.1016/j.camwa.2017.07.016.

[40] A. De Rosis, E. Lévêque, Central-moment lattice Boltzmann schemes with fixed and moving immersed boundaries, Comput. Math. Appl. 72 (6) (2016) 1616–1628.
[41] M. Rohde, D. Kandhai, J.J. Derksen, H.E.A. van den Akker, A generic, mass conservative local grid refinement technique for lattice-Boltzmann schemes, Internat. J. Numer. Methods Fluids 51 (4) (2006) 439–468.
[42] H. Chen, O. Filippova, J. Hoch, K. Molvig, R. Shock, C. Teixeira, R. Zhang, Grid refinement in lattice Boltzmann methods based on volumetric formulation, Physica A 362 (1) (2006) 158–167.
[43] M. Schönherr, K. Kucher, M. Geier, M. Stiebler, S. Freudiger, M. Krafczyk, Multi-thread implementations of the lattice boltzmann method on non-uniform grids for CPUs and GPUs, Comput. Math. Appl. 61 (12) (2011) 3730–3743.
[44] O. Filippova, D. Hänel, Grid refinement for lattice-BGK models, J. Comput. Phys. 147 (1) (1998) 219–228.
[45] A. Dupuis, B. Chopard, Theory and applications of an alternative lattice Boltzmann grid refinement algorithm, Phys. Rev. E 67 (6) (2003).
[46] D. Lagrava, O. Malaspinas, J. Latt, B. Chopard, Advances in multi-domain lattice Boltzmann grid refinement, J. Comput. Phys. 231 (14) (2012) 4808–4822.
[47] J. Tölke, M. Krafczyk, Second order interpolation of the flow field in the lattice Boltzmann method, Comput. Math. Appl. 58 (5) (2009) 898–902 Mesoscopic Methods in Engineering and Science.
[48] N. Pellerin, S. Leclaire, M. Reggio, An implementation of the Spalart - Allmaras turbulence model in a multi-domain lattice Boltzmann method for solving turbulent airfoil flows, Comput. Math. Appl. 70 (12) (2015) 3001–3018.
[49] J. Latt, B. Chopard, Lattice Boltzmann method with regularized pre-collision distribution functions, Math. Comput. Simulation 72 (2) (2006) 165–168.
[50] Q. Zou, X. He, On pressure and velocity boundary conditions for the lattice Boltzmann BGK model, Phys. Fluids 9 (6) (1997) 1591–1598.
[51] H. Xu, P. Sagaut, Analysis of the absorbing layers for the weakly-compressible lattice Boltzmann methods, J. Comput. Phys. 245 (2013) 14–42.
[52] S. Geller, M. Krafczyk, J. Tölke, S. Turek, J. Hron, Benchmark computations based on lattice-Boltzmann, finite element and finite volume methods for laminar flows, Comput. Fluids 35 (8) (2006) 888–897.
[53] H. Mansy, P.-M. Yang, D.R. Williams, Quantitative measurements of three-dimensional structures in the wake of a circular cylinder, J. Fluid Mech. 270 (1994) 277–296.
[54] D. Barkley, R.D. Henderson, Three-dimensional Floquet stability analysis of the wake of a circular cylinder, J. Fluid Mech. 322 (1996) 215–241.
[55] S.C.R. Dennis, G.-Z. Chang, Numerical solutions for steady flow past a circular cylinder at Reynolds numbers up to 100, J. Fluid Mech. 42 (03) (1970) 471.
[56] B. Fornberg, A numerical study of steady viscous flow past a circular cylinder, J. Fluid Mech. 98 (04) (1980) 819–855.
[57] X. He, G. Doolen, Lattice Boltzmann method on curvilinear coordinates system: Flow around a circular cylinder, J. Comput. Phys. 134 (2) (1997) 306–315.
[58] F. Nieuwstadt, H.B. Keller, Viscous flow past circular cylinders, Comput. Fluids 1 (1) (1973) 59–71.
[59] C.H.K. Williamson, Oblique and parallel modes of vortex shedding in the wake of a circular cylinder at low Reynolds numbers, J. Fluid Mech. 206 (1989) 579–627.
[60] M.-C. Lai, C.S. Peskin, An immersed boundary method with formal second-order accuracy and reduced numerical viscosity, J. Comput. Phys. 160 (2) (2000) 705–719.
[61] C. Liu, X. Zheng, C.H. Sung, Preconditioned multigrid methods for unsteady incompressible flows, J. Comput. Phys. 139 (1) (1998) 35–57.
[62] J.-I. Choi, R.C. Oberoi, J.R. Edwards, J.A. Rosati, An immersed boundary method for complex incompressible flows, J. Comput. Phys. 224 (2) (2007) 757–784.
[63] S. Mittal, T.E. Tezduyar, Massively parallel finite element computation of incompressible flows involving fluid-body interactions, Comput. Methods Appl. Mech. Engrg. 112 (1–4) (1994) 253–282.
[64] T. Imamura, K. Suzuki, T. Nakamura, M. Yoshida, Flow simulation around an airfoil by lattice boltzmann method on generalized coordinates, AIAA J. 43 (9) (2005) 1968–1973.
[65] A.A. Johnson, T.E. Tezduyar, Mesh update strategies in parallel finite element computations of flow problems with moving boundaries and interfaces, Comput. Methods Appl. Mech. Engrg. 119 (1) (1994) 73–94.

Please cite this article in press as: E.J. Falagkaris, et al., PROTEUS: A coupled iterative force-correction immersed-boundary multi-domain cascaded lattice Boltzmann solver, Computers and Mathematics with Applications (2017), http://dx.doi.org/10.1016/j.camwa.2017.07.016.